Universiteit Antwerpen

This item is the archived peer-reviewed author-version of:

Chemodynamics and bioavailability of metal ion complexes with nanoparticles in aqueous media

Reference:
van Leeuw en Herman P., Duval Jérôme F.L., Pinheiro José Paolo, Blust Ronny, Tow n Raew yn M..- Chemodynamics and bioavailability of metal ion complexes w ith nanoparticles in aqueous media
Environmental science : nano - ISSN 2051-8161 - 4:11(2017), p. 2108-2133
Full text (Publisher's DOI): https://doi.org/10.1039/C7EN00625J
To cite this reference: https://hdl.handle.net/10067/1469300151162165141

uantwerpen.be
Institutional repository IRUA

Chemodynamics and bioavailability of metal ion complexes with nanoparticles in aqueous media[§]

Herman P. van Leeuwen[1], Jérôme F. L. Duval[2,3], José Paulo Pinheiro[2,3], Ronny Blust[4], Raewyn M. Town*[1,4]

[1] Physical Chemistry and Soft Matter, Wageningen University & Research, Stippeneng 4, 6708 WE Wageningen, The Netherlands

[2] CNRS, Laboratoire Interdisciplinaire des Environnements Continentaux (LIEC), UMR 7360 CNRS, 15 avenue du Charmois, 54500 Vandoeuvre-les-Nancy, France

[3] Université de Lorraine, LIEC, UMR 7360 CNRS, 15 avenue du Charmois, 54500 Vandoeuvre-les-Nancy, France

[4] Systemic Physiological and Ecotoxicological Research (SPHERE), Department of Biology, University of Antwerp, Groenenborgerlaan 171, 2020 Antwerp, Belgium. Corresponding author, email: raewyn.town@uantwerpen.be

[§] We dedicate this article to our colleague Jacques Buffle (University of Geneva, Switzerland), who has played such an inspiring role in the development of the subject matter.

Abstract

Nanoparticles (NPs) exhibit unique reactivity features that stem from the spatial confinement of their reactive sites to the particle body, which typically carries electric charges. Accordingly, association of ions and molecules with NPs takes place in a local environment that may be very different from that prevailing in the bulk aqueous medium. We present a critical overview of a conceptual framework that describes the dynamic features of metal ion, M, association with different types of NPs, i.e. impermeable (hard, 2D), core-shell, and permeable (soft, 3D). The interpretation identifies the crucial role played by the particulate electric field, and elucidates the factors that determine which step in the overall association/dissociation process is the rate-limiting one. The scope encompasses delineation of the distribution of NP-associated metals, M-NP, over various intraparticulate forms, as well as description of the influence of the intraparticulate spatial distribution of reactants on the complex formation/dissociation kinetics. The connection between the chemodynamic features of M-NP entities at the intraparticulate level and their reactivity at the macroscopic scale is elaborated. These relationships are used to derive analytical expressions for the lability of M-NP entities at reactive interfaces, such as sensors and organisms. Such knowledge is required to make mechanistic links with bioavailability and ensuing toxicity. The interpretation includes formulation of the operational reaction layer at the macroscopic interface and the significance of partial size exclusion of the NP body therefrom. The concepts are illustrated by confrontation with sets of experimental data for different types of natural and engineered NPs.

A. Introduction

Over the past decade, the recognition of the special metal ion complexation features of particulate multisite ligands has initiated a detailed exploration of the underlying physicochemical processes. The preliminary observations on electrochemical lability of metal complexes with colloidal particles (typically in the size domain of order 100 nm)[1-4] were soon superceded by work on both hard and soft nanoparticles (denoted as NPs, typically of the order of 10 nm in size).[5-7] Perhaps the leading characteristic of such particulate complexants is the spatial confinement of the metal ion binding sites to the particle surface (hard particles, denoted as ‘2D’) or to the particle volume (soft and core-shell permeable particles, denoted as ‘3D’). Consequently, the reactive metal ions have to be transported from the surrounding medium to the particles

before they can undergo complexation. Effectively, this transport will be slower than the corresponding process for simple molecular complexants: depending on particle size, the transport rates may actually be orders of magnitude lower.[5] In connection with this, the particular kinetic features of NP binding sites can explain observations such as an apparent decrease in voltammetric lability of metal complexes sorbed to colloids as compared to a similar type of complex with a single-site ligand in solution.[2]

Particles dispersed in aqueous media generally carry electric charge, either as a surface charge (hard particles), a volume charge (soft particles), or a combination of the two e.g. in core/shell particles. A schematic view of the various particle types together with the various defining parameters is given in Fig. 1. A full list of symbols and abbreviations is provided at the end of the article.

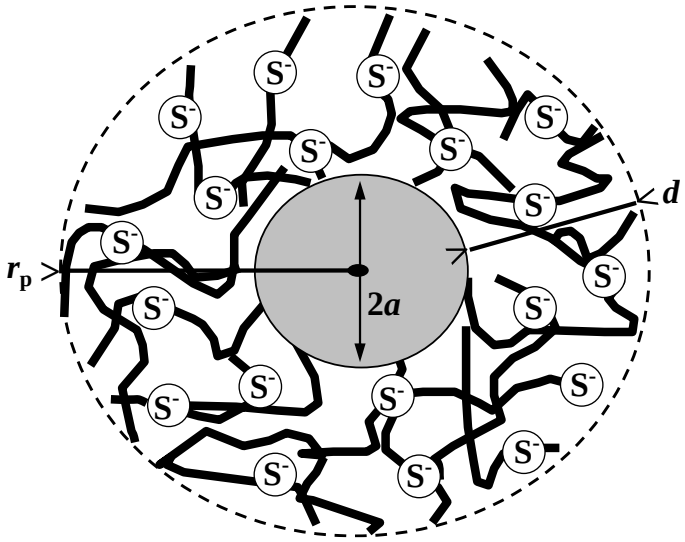

Fig. 1 Schematic view of a generic nanoparticulate complexant containing reactive sites, S, that are nominally shown as being negatively charged. Additional mere charges with no intrinsic chemical affinity for the target metal ion may also be present. The figure shows the setting for a core-shell NP with particle radius r_p, comprising a soft shell of thickness d and an impermeable core of radius a. At the hard (2D) particle limit, $d \rightarrow 0$ and all reactive sites are at the particle/medium surface; at the soft particle limit, $a \rightarrow 0$ and the reactive sites are distributed throughout the entire volume of the NP body. Adapted from Fig. 4 in ref. 5.

In all cases, the particles have their own physicochemical micro-environment at an electric potential where the ion concentrations and ionic strength generally differ from those in the medium. Thus, any complex formation/dissociation processes typically take place under conditions of coupling with ion redistribution

processes. For soft particles with a high water content, the spherical setting of the flux within the particle body means that the intraparticulate diffusion of the hydrated metal ion with charge z_M, $M_{aq}^{z_M}$, is generally fast compared to its diffusion from the particle surface to the bulk medium (mathematical proof is given in ref. 8). The overall reaction scheme for inner-sphere complex formation has been formulated in terms of an elaborated Eigen mechanism, as shown schematically in Fig. 2.

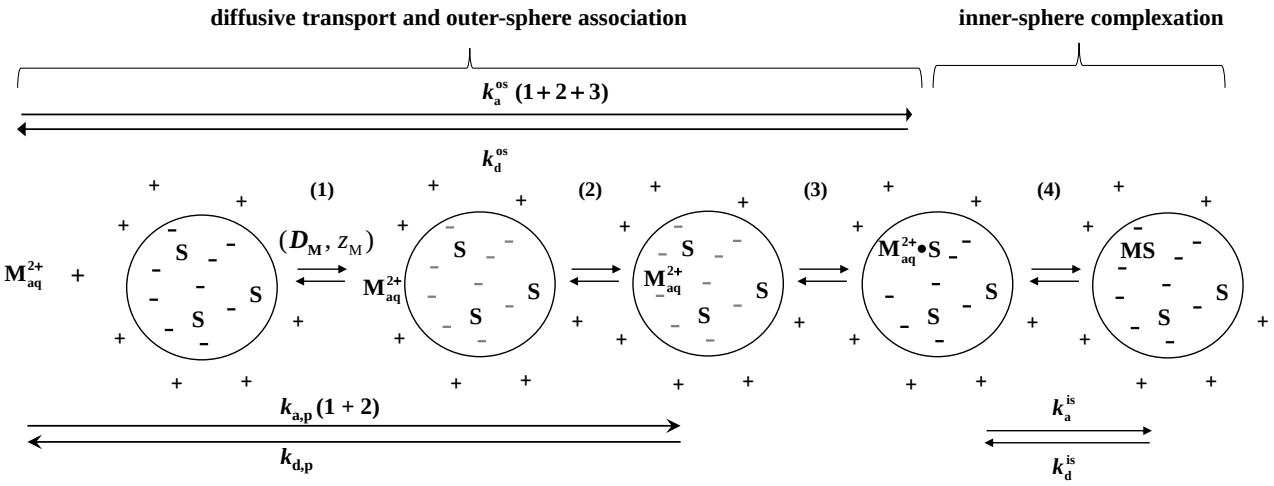

Fig. 2 Stepwise complexation of a hydrated divalent metal ion, M_{aq}^{2+} (diffusion coefficient, D_M), from the bulk medium with a nanoparticulate complexant containing charged or uncharged binding sites (S) and mere charges (-). For convenience, and without loss of generality, we show the example of a divalent metal ion; the conceptual framework is applicable to metal ions of any charge, z_M. The +'s around the particle denote the extraparticulate part of the counterionic atmosphere. In the case of impermeable NPs the sites and charges are restricted to the particle surface; for core-shell and soft NPs the sites and charges are distributed throughout the permeable zone (see Fig. 1). The association steps are (1) diffusion of M_{aq}^{2+} from the bulk solution to the surface of the complexant, (2) crossing the solution/particle interface and incorporation within the particle as a free hydrated ion, (3) outer-sphere association of M_{aq}^{2+} with S, resulting in M_{aq}^{2+}•S species, and (4) formation of inner-sphere complexes, MS, including the loss of water of hydration by M_{aq}^{2+} and formation of a chemical bond with site S. The various rate constants corresponding to the above steps are indicated with the subscript 'a' and 'd', denoting association and dissociation processes respectively. Figure is adapted from Fig. 1 in ref. 7.

For all types of charged particles, an electric double layer is encountered at the particle/medium interface. Typical for soft charged particles, is the occurrence of Donnan effects within the particle volume. Formation of inner-sphere complexes between metal ions from the medium and binding sites inside the permeable zone of the particle body lowers the intraparticulate magnitude of the charge density (except for situations where binding sites S are in sufficient overall excess over M, and the bulk M concentration is well below that of ions from the background electrolyte in the medium). All in all, the electric field of a complexing particle generally has far-reaching impact on the effective stability features and the chemodynamics of the metal complex. This is especially true for nanoparticulate complexants because in the nm domain all the relevant physicochemical length/time scales (particle size, diffusion layer thickness, chemical reaction layer thickness, electric double layer thickness) may be of similar magnitude, implying that the pertaining electrostatic and chemical relaxation processes will be strongly linked and indeed should be considered simultaneously.[9]

The chemodynamic features of metal complexes are generally described by the notion of lability, which embodies the interplay between diffusive mass transport and association/dissociation kinetics of the metal species in the context of an ongoing process at a macroscopic interface, e.g. accumulation of the free metal ion by a sensor or an organism. Lability of metal complexes has traditionally been linked to the reaction layer approach as developed by Brdička, Koutecký and Heyrovský circa 1950.[10-12] Their concept of lability is formulated for a homogeneous system in which the complexation partners are molecular-scale entities that are free to move in the aqueous medium. Obviously, reactive sites that are structural components of colloidal and nanoparticulate complexants do not possess such freedom. E.g. for soft NPs the mobility of the sites is limited by that of the whole particle body. Furthermore, an intraparticulate reaction layer is generally formed at the interface between the particle body and the surrounding medium.[13,14] This reaction layer controls the contribution of the inner-sphere complex MS to the dynamic exchange of the reactive M^{2+} with the surrounding medium.

Herein we comprehensively review the fundamental features of nanoparticulate complexants and the chemodynamics of the ensuing complex species. A generic theoretical framework is presented, and factors that influence the nature of the rate-limiting step in the overall association/dissociation reaction are discussed.

The scope of the assessment includes the characteristic features of the particles (e.g. size, permeability, charge density, chemical functionality) and of the metal ions (e.g. dehydration rate constant, chemical affinity). The interpretation is drawn to the level of the operational lability of nanoparticulate metal complexes at macroscopic reactive (bio)interfaces, e.g. a dynamic speciation sensor or an organism, and illustrated with practical examples.

B. Metal ion speciation equilibria in dispersions of complexing nanoparticles

Right from the outset we make the fundamental distinction between so-called *smeared-out* concentrations, which refer to the conventional concentrations for chemical species averaged over the entire volume of the solution/dispersion, and *local* concentrations, which may apply to spatial zones of nanoparticle bodies/surfaces or to the bulk medium upon equilibration with suspended nanoparticles. For nanoparticles, the local concentrations generally are the most pertinent since they govern the actual physicochemical conditions prevailing at the reactive sites. Still, conversion to smeared-out concentrations is unavoidable in the context of overall large scale features such as lability at a macroscopic reactive (bio)interface (see Section C5). Furthermore, unless otherwise stated, we shall primarily consider the case where a negatively charged NP is equilibrated in 1-1 non-complexing background electrolyte, with a concentration well in excess over the smeared-out concentration of charged sites. In turn, the latter is assumed to be in large excess over the target divalent cation, M^{2+}, i.e. we consider the regime of low coverage of binding sites by M^{2+}. These conditions are typically met for the case of trace metal ions in environmental and biological media. In this context we note that typical divalent electrolyte ions, such as Ca^{2+} and Mg^{2+}, contribute only to the establishment of the particulate electric field and do not have significant intrinsic chemical affinity for the reactive sites.[15-19] Also, we shall generally consider dilute dispersions for which the total volume fraction of the NPs is much less than unity.

Before proceeding to elucidating the chemodynamic features of M-NP associates, we first outline concepts for describing the nature and stability of the various forms of M that are associated with NPs, i.e. the details of the intraparticulate metal speciation. Measurements and interpretations of metal ion binding by negatively charged NPs are often involved with distinction between the “bound” and “free” metal ions, e.g. by ion selective

electrode potentiometry in the bulk solution phase. The corresponding *apparent* stability constant, K_{app}, is then defined as:

$$K_{app} = \bar{c}_{MNP} / c_M^* \bar{c}_S \quad (1)$$

where c_M^* is the concentration of M_{aq}^{2+} in the bulk aqueous medium, $\bar{c}_S$ is the smeared-out concentration of free reactive sites (which at low metal to site ratio approximates the total site concentration, $\bar{c}_{S,t}$), and $\bar{c}_{MNP}$ is the sum of the smeared-out concentrations of all forms of M that are associated with the NP. The extent to which M associates with an NP is determined by both electrostatic and intrinsic chemical contributions to the binding. That is, some of the M^{2+} associated with the negatively charged NP may be in the form of an electrostatically generated excess of "free" ions within the liquid micromedium of the particle body/surface. Obviously this would turn into a repulsive deficit of free metal ions in the case of positively charged NPs. Accordingly, K_{app} values certainly do not reflect the true nature of inner-sphere MS complexes. Translation of K_{app} values to intrinsic chemical stability constants, K_{int}, requires careful accounting for the various electrostatic contributions to metal ion binding.

Different types of nanoparticulate potential profiles are distinguished based on the relative magnitude of the charge separation distance, ℓ_C, as compared to the Debye screening length in the medium, κ^{-1}.[5] In the *low charge density* regime, $\ell_C >> \kappa^{-1}$ and the potential at a given charged site is dominated by its local coulombic field (see the potential profile sketched in Fig. 3(b)). In the *high charge density* regime, $\ell_C << \kappa^{-1}$, the cooperative electrostatic forces of the many adjacent sites yields a potential that is much greater than the primary coulombic interaction at an individual site (Fig. 3(a)). Between these extremes, we identify the *intermediate charge density* regime, for which $\ell_C \approx \kappa^{-1}$; both the local coulombic term and the cooperative electrostatics then count.

Depending on the size, charge density, and permeability (softness) of the NP, electrostatic contributions to metal ion association may include Poisson-Boltzmann accumulation in the extra- and intraparticulate double-layer, Donnan-type partitioning in the bulk of the soft particle body, and counterion condensation governed by cooperative electrostatics in the strongly charged intraparticulate double-layer zone.[17-19] Outer-sphere M_{aq}^{2+} --

S^- ion pairing may occur at the particle surface and throughout the particle body; for particles in the "high charge density" regime (see Fig. 3) this is of an essentially stochastic nature.[5] The *equilibrium* stability constant K^{os} for the outer-sphere

M_{aq}^{2+} ●S reactant pair compares M_{aq}^{2+}, with its fully intact inner hydration sphere in contact with S, to M_{aq}^{2+} at the potential of the bulk medium (*cf.* Fig. 2). It is given by:[20]

$$K^{os} = \tfrac{4}{3}\pi a_{os}^3 N_{Av} \exp(-\boldsymbol{U}) \qquad (2)$$

where a_{os} is the center-to-center distance between reactants in the outer-sphere reactant pair, N_{Av} is the Avogadro number, and $\boldsymbol{U}$ is the applicable electric energy (see Section C2). In the low charge density regime for nanoparticles (and for small ions/molecules), $\boldsymbol{U}$ is the individual ion pair interaction energy, $\boldsymbol{U}^{os}$, which is essentially of a coulombic nature. The features of these different types of electrostatic contribution and the conditions under which they prevail will be elaborated in Section C2.

For highly charged NPs, several different types of electrostatic contributions may be operative. Counterion condensation is a well-known phenomenon that was originally developed to describe the tendency of a highly charged linear polyelectrolyte to condense counterions in its immediate vicinity.[21,22] The phenomenon is applicable to any geometry so long as the structural charge density is beyond a certain limiting value. Thus we can envisage counterion condensation to be operative at the NP/medium interface of highly charged 2D and 3D NPs. For the case of soft 3D NPs, a two-state Counterion Condensation-Donnan (CCD) model has recently been developed as the first approach to take into account the highly charged interfacial double layer.[17-19]The approach was inspired by the observation that for large soft NPs mere Donnan partitioning significantly underestimates the extent of binding of Ca^{2+}, an ion without significant inner-sphere complexation affinity. The CCD model combines (i) Donnan partitioning within the bulk of the soft NP body (with a volume V_D, and volume fraction in the dispersion φ_D) with (ii) electric condensation of target metal ions M^{2+} in the strongly charged part of the particle volume, i.e. in the intraparticulate zone of the double layer (DL) at the particle/medium interface (with thickness ℓ_{DL}, volume V_{DL}, volume fraction in the dispersion φ_{DL}, and a condensation limit for 2+ counterions $\overline{f}_C$ which defines the extent to which the structural charge is compensated by condensed ions). A schematic view of the electrostatic setting for a soft NP under conditions

where r_p is much larger than the double layer thickness, κ^{-1}, in the high and low charge density regimes is shown in Fig. 3.

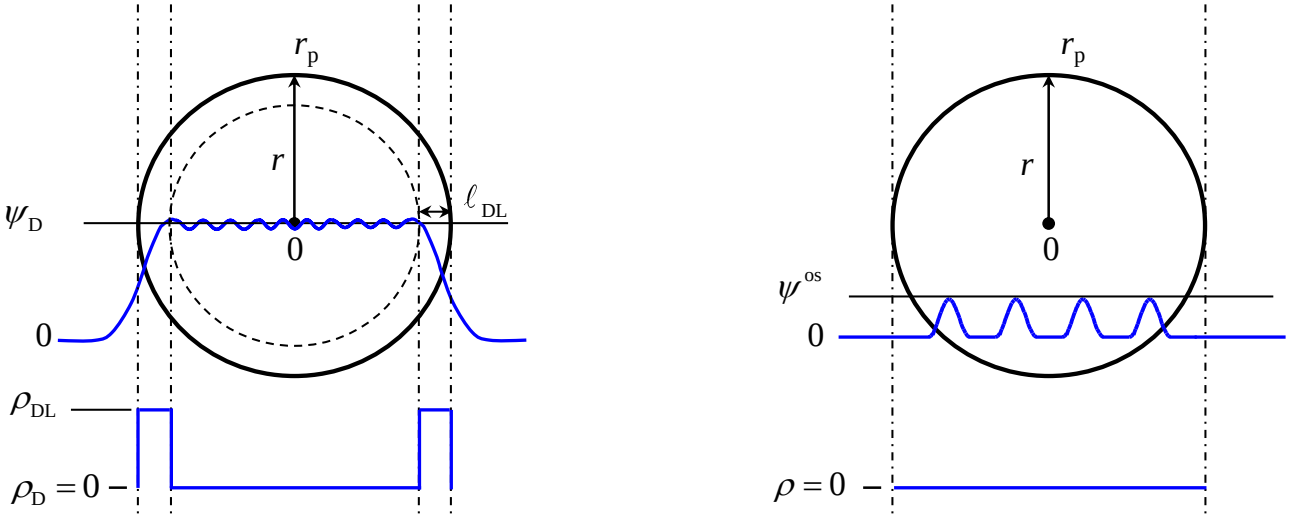

(a) (b)

Fig. 3 Schematic representation of the electrostatic conditions prevailing within a soft spherical nanoparticle with radius r_p and charge separation distance, ℓ_C, for (a) the high charge density case ($r_p > \kappa^{-1} > \ell_C$), with the pertaining two-state electrostatic model where ℓ_{DL} is the condensation layer thickness, and (b) the low charge density case ($r_p > \ell_C > \kappa^{-1}$). The model parameter ℓ_{DL} is related to the intraparticulate screening length κ_p^{-1}, which is immaterial in the low charge density regime. The true profile of the potential, ψ, is shown in blue through the NP, with ψ_D in the high charge density case corresponding to the average of the rippled profile and ψ^{os} in the low charge density case corresponding to the maxima of the local potential field around an individual site; $\psi = 0$ for the bulk medium. The intraparticulate profile of the charge density, ρ, (with contributions from electrolyte ions and structural immobile charges carried by the NPs) is sketched in blue below the NP; the profile of ρ in the extraparticulate double layer in the medium is of a classical diffuse nature. In the case of negatively charged NPs, ψ_D, ψ^{os}, and ρ_{DL} have a negative sign. Redrawn after Fig. 1 in ref. 18.

The differentiated CCD electrostatic model enables proper definition and utilization of the intrinsic stability constant in terms of intraparticulate conditions and reactant species concentrations. For the high charge density

case, the applicable K_{int} within the bulk Donnan volume V_D (if applicable, depending on NP size and medium salinity conditions) of the NP is given by:

$$K_{int} = \frac{c_{MS}^{D}}{c_{M}^{D} c_{S}^{D}} \quad (3a)$$

where c_{MS}^{D}, c_{M}^{D} and c_{S}^{D} are the local *intraparticulate* average concentrations of inner-sphere complexes, free metal ions and reactive sites in V_D, respectively. In the high charge density regime, the outer-sphere volume around a complexing site and the remaining aqueous volume of the particle practically are at the same potential.[5] In such a case the intraparticulate free metal ion and the outer-sphere associates are electrostatically nearly equivalent and interconversion between these species is very fast. Accordingly, most of the ion pairing energy is accounted for in the energy change that occurs when M enters the particle, i.e. the electrostatic Boltzmann partitioning factor, $\overline{f}_B$ (see Section C2.2). Similarly, within the double layer zone of a highly charged particle the condensed ions and the free M will have comparable energy levels. In such case the condensed M^{2+}, M_{cond}, will count explicitly in K_{int}, i.e.:

$$K_{int} = \frac{c_{MS}^{DL}}{(c_{M}^{DL} + f^{DL} c_{M,cond}^{DL}) c_{S}^{DL}} \quad (3b)$$

where the superscript DL denotes the average concentrations of the various M species in the DL, and f^{DL} is a pre-factor with magnitude of unity in the high charge density regime. For particles with lower charge density there will be a finite and significant energy difference between the condensed and free M (Fig. 3). The f^{DL} in eqn (3b) will then be greater than unity since the condensed ions will have the lower energy level. Note that on passing from high to low charge density domains, the cooperative electrostatics of condensation gradually evolve into individual ion pair behaviour, as e.g. applicable in the well-known Eigen mechanism for aqueous complex formation reactions.[23] Within the DL zone the metal speciation will be a function of position due to the potential gradient and the ensuing gradient in the concentration of free M_{aq}^{2+}. Generally, within the DL of a highly charged NP complexant, the sum of $c_{M,cond}^{DL}$ and c_{MS}^{DL} will be much greater than c_{M}^{DL}.[24]

The consequences of intraparticulate metal speciation for the chemodynamic features of M-NP entities are elaborated in Section C. Practical strategies for elucidation of the distribution of M over its various intraparticulate forms, and illustrative results, are given in Section D.

C. Dynamic features of metal ion complexation by nanoparticles

This section describes the *relevant physicochemical rate-controlling equilibration processes* involved in the metal ion binding by NP complexants. The conceptual framework accounts for variation with size and charge density of the particles, and distinguishes between inner-sphere and outer-sphere association (Fig. 2). The involved processes comprise chemical relaxation, physical relaxation, and the coupling between these processes as elaborated below.

C1 Chemical relaxation

This section discusses the factors that contribute to the rates of inner-sphere complex formation and dissociation. The expressions are explicit in terms of the *intraparticulate* conditions and are formulated on a per site basis. Furthermore, for simplicity of reasoning we initially consider the situation where the Boltzmann distribution of charged species between the bulk medium and the particle is established so rapidly that equilibrium may be invoked (see Section C2). That is, a constant steady-state concentration of the outer-sphere associate, $M^{2+}_{aq}\bullet S$, is assumed to be attained before significant inner-sphere complex formation takes place.

The inner-sphere complex formation step takes place once the hydrated metal ion is in the outer-sphere associate position; step 4 in Fig. 2. In most cases, the rate limiting process in this step is the elimination of water from the inner hydration shell of M. For such cases, the limiting rates of the inner-sphere association and dissociation are formulated as follows:

Soft and permeable (3D) particles.

For a soft and permeable nanoparticle, the limiting rate of inner-sphere complex formation R_a^{is}, from the precursor reactive species $M^{2+}_{aq}\bullet S$ is given by:[25]

$$R_a^{is} = k_w c_{M\bullet S} \qquad [\text{mol m}^{-3}\ \text{s}^{-1}] \qquad (4)$$

where k_w is the inner-sphere dehydration rate constant of M_{aq}^{2+}, and $c_{M\bullet S}$ is the intraparticulate concentration of the outer-sphere associates. As noted above, in the high charge density limit, the M in an outer-sphere associate $M_{aq}^{2+}\bullet S$ is electrostatically equivalent to the intraparticulate free M_{aq}^{2+}. Then the concentrations $c_{M\bullet S}$ and c_M are simply related via the total outer-sphere volume fraction $N_S V^{os}/V_p$, where N_S is the number of reactive sites per particle, V^{os} is the volume around an individual site S that allows for formation of an outer-sphere associate (e.g. ion pair) with M_{aq}^{2+}, V_p is the volume of a particle body, and c_M is the intraparticulate concentration of M_{aq}^{2+}. Accordingly, R_a^{is} can be re-written as:

$$R_a^{is} = k_w (N_S V^{os}/V_p)\, c_M \qquad [\text{mol m}^{-3}\ \text{s}^{-1}] \qquad (5)$$

The intraparticulate concentration of S, c_S, is given by $N_S / N_{Av} V_p$, and thus we can write:

$$R_a^{is} = k_w V^{os} N_{Av} c_M c_S \qquad [\text{mol m}^{-3}\ \text{s}^{-1}] \qquad (6)$$

Whilst M_{aq}^{2+} may lose one or more water molecules upon inner-sphere complex formation, it is loss of the first H_2O molecule from the inner hydration layer that has the lowest rate constant k_w. As shown in eqn (6), the eventual rate of inner-sphere complex formation derives from k_w (an intrinsic property of the hydrated metal ion) and the pertaining intraparticulate conditions. Values for k_w are documented for many metal ions, and encompass a very wide range, e.g. for Ni(II), k_w is of the order 10^4 s^{-1}, whilst for Pb(II) it approaches 10^{10} s^{-1}.[26] The corresponding rate constant follows from eqn (6):

$$k_a^{is} = k_w V^{os} N_{Av} \qquad [\text{m}^3\ \text{mol}^{-1}\ \text{s}^{-1}] \qquad (7)$$

When the dissociation rate is controlled by inner-sphere dissociation, the rate derives straightforwardly from k_a^{is} and K_{int}:

$$R_d^{is} = \frac{k_a^{is}}{K_{int}} c_{MS} \qquad [\text{mol m}^{-3}\ \text{s}^{-1}] \qquad (8)$$

where k_a^{is} is given by eqn (7), and c_{MS} is the intraparticulate concentration of MS. The rate constant for inner-sphere dissociation, k_d^{is}, follows as

$$k_d^{is} = k_a^{is} / K_{int} = k_w V^{os} N_{Av} / K_{int} \qquad [\text{s}^{-1}] \qquad (9)$$

Hard and impermeable (2D) particles.

For case of a solid particle with reactive sites constrained to the particle surface, a 2D analogue of the Eigen mechanism may apply.[27] For such particles in the high charge density regime, the rate of the inner-sphere complexation step can be written as:

$$R_a^{is} = k_a^{is} \Gamma_S \Gamma_M A / V \qquad [\text{mol m}^{-2}\ \text{s}^{-1}] \qquad (10)$$

where A is the nanoparticulate surface area per unit volume V of dispersion, and Γ_M and Γ_S are the local (surface) concentrations of the free M_{aq}^{2+} and the reactive sites, respectively (mol m^{-2}), applicable at Boltzmann equilibrium. The corresponding rate constant can be expressed in a manner equivalent to that for the 3D case, i.e. eqn (7).

Analogous to the reasoning for soft particles, the high charge density regime for hard particles corresponds to the situation in which the surface site density is so high that the smeared-out potential overrules the local potential profile of an individual site. This would imply that the outer-sphere surface layer should have a thickness on the order of the diameter of the hydrated metal ion. For the case of a large excess of reactive sites over bound metal ion (low coverage by M), and the transport of M_{aq}^{2+} to the surface is sufficiently fast, the surface concentration of MS, Γ_{MS}, is linearly related to the surface concentration of free M_{aq}^{2+}, Γ_M, via the so-called Henry coefficient, K_H.

$$\Gamma_{MS} = K_H \Gamma_M A / V \qquad [\text{mol m}^{-2}] \qquad (11)$$

It follows that the rate constant for dissociation of an inner-sphere surface complex can be written as:

$$k_d^{is} = k_a^{is} \Gamma_S \Gamma_M (A/V) / \Gamma_{MS} = k_a^{is} \Gamma_S / K_H \qquad [\text{s}^{-1}] \qquad (12)$$

A general observation for all types of NPs is that the particle electric field implicitly contributes to the magnitude of R_a^{is}: the higher the electric field, the greater is the local concentration of the precursor outer-sphere associate. For a given charge density, R_a^{is} is constant beyond a certain minimum r_p, i.e. when the equilibrium Donnan partitioning between extraparticulate free M and outer-sphere associates is achieved. At the onset of the NP regime, i.e. r_p values on the order of 1 nm, R_a^{is} increases somewhat with increasing r_p.[7]

This effect reflects the physical limitations to the accumulation of M at/within the NP surface/body. That is, for r_p less than *ca*. 10 nm Boltzmann accumulation pertains mostly to the extraparticulate counter ion atmosphere, within which some of the accumulated M_{aq}^{2+} may lie at an appreciable distance from the NP surface.[28] Further features of the particle electric field are detailed in the following section C2 below.

C2 Physical relaxation

When a reactive metal ion is introduced into an aqueous dispersion of NPs, a number of electric relaxation processes take place as M_{aq}^{2+} responds to the particulate electric field. The magnitude of the electric field influences the rate of diffusion of M_{aq}^{2+} towards/away from the NP as well as the extent of its accumulation within the extraparticulate ionic atmosphere and the NP body/shell/surface as applicable. The greater the density of electric charges carried by the nanoparticle, the larger the time constant for setting up the ionic distribution equilibrium with the medium. Compared to a monovalent cation, a higher valency cation ($z_M > 1$) will accumulate more strongly within/around the body of a soft/hard nanoparticle with negative structural charge. The rate of accumulation is generally governed by diffusion and proceeds until Boltzmann partition equilibrium between the charged NP body/surface and the ions in the medium is attained. For cations that can also form inner-sphere complexes with the reactive sites, the electrostatic accumulation proceeds in conjunction with outer-sphere and inner-sphere complex formation. In case of transition metal ions with moderate to fast dehydration rates, e.g. Cd^{2+}, Pb^{2+}, Cu^{2+},[26] the electric relaxation towards a fully equilibrated ionic distribution equilibrium between the NP and the bulk aqueous medium may well be the slower step in the overall metal/NP complexation process.[9]

It was recently shown that the Eigen mechanism may well apply to aqueous soft[6] and hard[27] nanoparticulate complexants. Thus, for the limiting cases of low and high bulk charge densities, the expressions of the rate constants for the *intraparticulate* outer-sphere and inner-sphere association and dissociation steps should apply (see Section C1). The chemodynamic framework developed,[5,6] demonstrates that particle shape/size, reactive site density, and charge density are key determinants of the pertaining relaxation parameters.

The reasoning below largely refers to the example case of soft, permeable NPs. In line with usual practice, it is assumed that the nanoparticulate electric potential profile with respect to the bulk medium is pre-established by the indifferent electrolyte ions. The slower accumulation of higher valency target ions then occurs under the influence of this preset potential field. We firstly consider the situation where charged and reactive sites are homogeneously distributed within the NP body and the rate constants are expressed in terms of intraparticulate conditions on a per site basis; the effects of spatial discretization are subsequently addressed in section C3.

C2.1 Impact of the electric field on the diffusive supply and outer-sphere steps in the overall complex formation process

The rate constant $k_{a,p}$ in Fig. 2 merely represents the electric association between M_{aq}^{2+} and the charged complexing NP entity. It is a diffusive rate constant, including the conductive acceleration by the electrostatic field encountered over the diffusion path [see section C3 for details]. The diffusive flux towards the spherical NP body is of a steady-state nature for times beyond the order of r_p^2 / D_M. The Smoluchowski-Debye treatment of $k_{a,p}$ is based on steady-state limiting diffusion,[29-32] and for r_p values of the order of 10 nm or greater the classical equation can be written as:

$$k_{a,p} = (4\pi N_{Av} r_p D_M / N_S) \boldsymbol{U} / [\exp(\boldsymbol{U}) - 1] \qquad [m^3\ mol^{-1}\ s^{-1}] \qquad (13)$$

with corresponding rate, $R_{a,p}$:

$$R_{a,p} = (4\pi N_{Av} r_p D_M / N_S)(\boldsymbol{U} / [\exp(\boldsymbol{U}) - 1]) c_M^* c_S \qquad [mol\ m^{-3}\ s^{-1}] \qquad (14)$$

where D_M and D_p are the diffusion coefficient of the metal ion and the particle, respectively. In the case of a positively charged metal ion and a negatively charged NP, the factor $\boldsymbol{U} / [\exp(\boldsymbol{U}) - 1]$ is greater than unity and represents the conductive accelerating coefficient ($\boldsymbol{U} < 0$) in the diffusive transport of M_{aq}^{2+} towards the particle. It is based on simple coulombic interaction between the charged particle and the incoming ion. In section C3, this accelerating factor is developed to an NP-volume averaged coefficient, denoted $\overline{f}_{el,a}$, which results from the full integration over the potential profile across the NP/medium interface for dedicated integration borders. The relevant electric energy $\boldsymbol{U}$ is given by $\boldsymbol{U} = z_M^+ F\psi / RT$, with ψ being the *position-dependent* electric

potential in/around the particle. Proceeding with the NP-volume averaged coefficient, the corresponding limiting rate of diffusion of free M_{aq}^{2+} from the spherical particle body into the medium, $R_{d,p}$, is given by:

$$R_{d,p} = \frac{3D_M \overline{f}_{el,d}}{r_p^2} c_M \qquad [\text{mol m}^{-3}\ \text{s}^{-1}] \qquad (15)$$

where $\overline{f}_{el,d}$ (= $\overline{f}_{el,a}$ / $\overline{f}_B$) is the coefficient for conductive diffusion from the NP body into the medium for the case where the electric fields in/around the NP are fully relaxed, and $\overline{f}_B$ denotes the integral average of $f_B(r)$ over the applicable NP volume for an assumed preset electric field.[33] For the case of a negatively charged NP and a positively charged reactant ion M_{aq}^{2+}, $\overline{f}_{el,d}$ is less than unity.

The corresponding diffusion-controlled rate constant, $k_{d,p}$, for 3D NPs is given by:

$$k_{d,p} = 3D_M \overline{f}_{el,d}(1 + K_{int}^{3D} c_S) / r_p^2 \qquad [\text{s}^{-1}] \qquad (16)$$

where K_{int}^{3D} is the intrinsic stability constant of the inner-sphere complex ($\text{m}^3\ \text{mol}^{-1}$). For 2D NPs, $k_{d,p}$ can be written as:

$$k_{d,p} = 3D_M \overline{f}_{el,d}(1 + K_{int}^{2D} \Gamma_S) / r_p^2 \qquad [\text{s}^{-1}] \qquad (17)$$

where K_{int}^{2D} has units $\text{m}^2\ \text{mol}^{-1}$.

For the case of a soft nanoparticle with a sufficiently large aqueous volume fraction, the fully hydrated M_{aq}^{2+} generally enters the particle body. If the extraparticulate counter charge (inside the diffuse double layer at the medium side of the NP/medium interface) is negligible compared to the intraparticulate counter charge, the relevant partitioning of M_{aq}^{2+} is that between the total outer-sphere volume $N_S V^{os}$ and the remaining particle volume (V_p - $N_S V^{os}$). Then the rate constant for outer-sphere association, k_a^{os}, derives from the expression for $k_{a,p}$, eqn (13), by accounting for the distribution of the incoming M_{aq}^{2+} between the outer-sphere volume and the remaining particle body volume (Fig. 2). The resulting expressions for k_a^{os} (per site S) for the high charge density limit (eqn 18a) and the low charge density limit (eqn 18b) are:[9]

$$k_a^{os} = 4\pi N_{Av} r_p (D_M + D_p) \frac{V^{os}}{V_p} \frac{\boldsymbol{U}_p}{\exp(\boldsymbol{U}_p) - 1} \qquad \text{high charge density regime} \quad [\text{m}^3\ \text{mol}^{-1}\ \text{s}^{-1}] \qquad (18a)$$

$$k_a^{os} = 4\pi N_{Av} r_p (D_M + D_p) \frac{\exp(-\boldsymbol{U}^{os}) V^{os}}{[\exp(-\boldsymbol{U}^{os}) - 1] N_S V^{os} + V_p} \qquad \text{low charge density regime} \quad [\text{m}^3\ \text{mol}^{-1}\ \text{s}^{-1}] \qquad (18b)$$

In the high charge density case, the magnitude of $\boldsymbol{U}_p$ is determined by the average electrostatic potential difference between the particle body and the bulk medium, $\overline{\psi}_p$ ($\boldsymbol{U}_p = z_M F \overline{\psi_p} / RT$).

The corresponding outer-sphere complex *dissociation* rate constant for soft nanoparticles is obtained from k_a^{os} / K^{os} using eqns (2), (18a), and (18b):[9]

$$k_d^{os} = 3 \frac{r_p}{a_{os}^3} (D_M + D_p) \frac{V^{os}}{V_p} \frac{\boldsymbol{U}_p}{1 - \exp(-\boldsymbol{U}_p)} \qquad \text{high charge density regime} \qquad [\text{s}^{-1}] \qquad (19a)$$

$$k_d^{os} = 3 \frac{r_p}{a_{os}^3} (D_M + D_p) V^{os} \Big/ ([\exp(-\boldsymbol{U}^{os}) - 1] N_S V^{os} + V_p) \qquad \text{low charge density regime} \qquad [\text{s}^{-1}] \qquad (19b)$$

For NPs with $r_p/a_{os} >> 1$ and the site number small enough to warrant that $V_p >> N_S V^{os}$, these equations reduce to:

$$k_d^{os} = \frac{3 D_M}{r_p^2} \frac{\boldsymbol{U}_p}{1 - \exp(-\boldsymbol{U}_p)} \qquad \text{high charge density regime} \qquad [\text{s}^{-1}] \qquad (20a)$$

$$k_d^{os} = \frac{3 D_M}{r_p^2} \qquad \text{low charge density regime} \qquad [\text{s}^{-1}] \qquad (20b)$$

Eqn (20b) confirms that for low charge densities k_d^{os} approaches the conventional rate constant for diffusive release from an uncharged sphere of radius r_p, i.e. $3D_M / r_p^2$.[9,34]

C2.2 Characteristic time constants for electric relaxation

With regard to electric relaxation, two basic time scales are distinguished. Firstly, pertaining to ionic transport in the electric double layer at the particle/medium interface, the time scale for relaxation of electrically charged zones in/around dispersed NPs in liquid media is given by the characteristic time $\tau = 1 / D\kappa^2$, a well-known key parameter in double-layer relaxation at electrode/solution interfaces[35,36] or in dispersions of charged hard

colloids.[37] Secondly, related to the diffusive transport of ions to and from each side of the particle, the relaxation time constant for M_{aq}^{2+} to reach equilibrium with an extraparticulate ionic atmosphere is typically on the order of r_p^2 / D_M. Thus for a small NP with r_p *ca.* 1 nm, relaxation times are of the order 10^{-9} s. This timescale is inside the $1/k_w$ regime of rapidly dehydrating metal ions such as $Pb(H_2O)_6^{2+}$ and $Cu(H_2O)_6^{2+}$, implying that for such metal ions the equilibration of the electric double layer at the NP/medium interface occurs at timescales comparable to that for inner-sphere complex formation. The consequence is that these two types of relaxation processes, both involving the target metal ion, will to some extent be coupled (See Section C3 below).

For particles with high charge densities and a radius well above the Debye length ($\kappa r_p >> 1$), establishment of the fully equilibrated NP/medium counterion distribution takes more time than for the low charge density regime, especially if counterions with valencies different from those of the background electrolyte are involved.[38] Consequently, for mixed electrolytes the composition in a charged zone, such as an interfacial double layer, differs from that in the bulk medium. In case of a trace metal ion M_{aq}^{2+} and a 1:1 background electrolyte A^+/B^-, the M_{aq}^{2+} will accumulate much more strongly than does A^+ in the vicinity of the negatively charged entities. The extent of accumulation is simply given by the pertaining Boltzmann equilibrium factor, $\overline{f}_B$:[39]

$$\overline{f}_B = c_M / c_M^* = \exp(-z_M F\psi / RT) = \exp(-\boldsymbol{U}) \qquad (21)$$

where the applicable electric potential ψ depends on the nature of the entity involved, e.g. for the bulk of a Donnan particle it is $\overline{\psi}_p$, and for a hard NP it is the surface potential ψ^s. The overbar notation denotes that the parameter is averaged over the applicable spatial domain. For a Donnan particle, $\overline{\psi}_p$ corresponds to a Donnan potential, ψ_D, given by:

$$\psi_D = \frac{RT}{zF}\operatorname{asinh}\left(\frac{\rho_p}{2zFc^*}\right) \qquad [V] \qquad (22)$$

where $z_- = z_+ = z$ is the valence of the symmetrical excess background electrolyte with bulk concentration c^*, ρ_p is the volume charge density due to charged groups on the backbone of the soft body, and other constants have their usual meaning. M_{aq}^{2+} will accumulate within the particle body until the intraparticulate concentration of free M_{aq}^{2+}, c_M, reaches $\overline{f}_B$ times that in the bulk medium.

For nanoparticles, under conditions of zero c_M in the particle at $t = 0$, and insignificant depletion of the bulk solution (i.e. sufficiently dilute NP dispersion), the time evolution of the metal concentration at the medium side of the particle/medium interface under steady-state diffusion conditions can be expressed as:

$$c_M^0(t) = c_M^*[1 - \exp(-t/\tau)] \qquad [\text{mol m}^{-3}] \qquad (23)$$

with τ the characteristic time constant for the soft particle case:

$$\tau = \frac{\overline{f}_B r_p^2}{3(D_M + D_p)} \qquad [\text{s}] \qquad (24)$$

which reduces to $\tau = \overline{f}_B r_p^2 / 3D_M$ for sufficiently large NPs. Thus the concentrations of $M_{aq}^{2+}\bullet S$ and free M_{aq}^{2+} inside the charged entity grow with time according to an exponential $[1 - \exp(-3Dt / r_p^2 \overline{f}_B)]$ dependence with $D = D_M + D_p$. Compared to the case without accumulation, the relevant rate constant, $k = 1/\tau = 3(D_M + D_p)/r_p^2$, is modified by the factor $1/\overline{f}_B$. Ions with high valencies feature large $\overline{f}_B$ values, that is long equilibration times to achieve the strong accumulation. The equilibrium ion distribution in the double layer at the particle/medium interface features a *finite* net charge density as prescribed by the interfacial electrostatics. On the other hand, a *zero* net charge density is ultimately attained within an equilibrated Donnan phase. In the case of counterion condensation in the intraparticulate double layer (section B), the applicable $\overline{f}_B$ is modified by the charge reduction imposed by the condensed counterions.[17-19]

C3 Coupling between different types of relaxation

This section extends the concepts presented in Section C2 and elaborates a general case involving coupling between extraparticulate diffusion of free metal ions and intraparticulate outer-sphere metal complex formation. We proceed for the general case of metal ions of valency z_M. Attention is now paid to the effects

of discretization, i.e. the spatial distribution of NP reactive sites within the particle body. A key aspect is the formulation of the partitioning function of intraparticulate free $M_{aq}^{z_M}$ between the outer-sphere binding site volume and the remaining particle volume, as a function of the intraparticulate electric field. The relevant factors are the distribution of sites and the ratio between the average site-to-site distance $< \ell_S >$ and the Debye length. To best capture the inherent dispersity of the reactivity, the rate constants are now expressed *per particle* (*cf.* the per site formulation used in previous sections) unless otherwise specified. For simplicity, it is assumed that the structural charges are carried only by the metal binding sites, $S_{i=1,...,N_S}$, each having an outer-sphere radius r^{os} and volume V^{os}. Without loss of generality, the expressions can be modified to include cases where the intraparticulate distribution of mere charges differs from that pertaining to M binding sites. More specifically, we review the various expressions that define the kinetic constants for outer-sphere complex formation in the reactive shell, k_a^{os}, and diffusive supply of $M_{aq}^{z_M}$ to the NP surface, $k_{a,p}$. The interpretation assumes that the inner-sphere complex formation step (Fig. 2) is infinitely fast and never overall rate-limiting.

C3.1 General expression for k_a^{os}

Consistent with the earlier sections, we consider the classical case in which complexation of the metal ion takes place after the intraparticulate field is already established by the excess background electrolyte. Starting from the pristine situation (t = 0) in which metal ions $M_{aq}^{z_M}$ are still absent from the reactive particle shell and the extraparticulate metal concentration equals the initial bulk value c_M^*, the kinetic constant $k_{a,i}^{os}$ for the outer-sphere association at time t>0 between a metal ion M and a metal binding site S_i in the shell can be formulated *via* the integration of the *local* metal flux $\boldsymbol{j}(\boldsymbol{r},t)$ (mol m^{-2} s^{-1}) of $M_{aq}^{z_M}$ across the outer sphere surface area A_i^{os} of S_i *via*

$$k_{a,i}^{os}(t) = -\oiint \boldsymbol{j}(\boldsymbol{r},t)\boldsymbol{n_i}(\boldsymbol{r})\mathrm{d}A_i^{os} / c_M^* \qquad [\mathrm{m^3\ s^{-1}}] \qquad (25)$$

where the double integral represents the integration over the entirety of the outer-sphere zones of reactive sites S_i located in the particle shell; bold characters correspond to vector entities and $\boldsymbol{n_i}(\boldsymbol{r})$ is the (dimensionless) vector perpendicular to the surface of ligand S_i. Under conditions of steady-state diffusive supply from the

medium to the NP, *i.e.* at timescales much longer than those required for development of a diffusion layer around the NP (see section C2.2), the rate constant k_a^{os} for the outer-sphere association of $M_{aq}^{z_M+}$ with the NP ligand as a whole is given by:[40]

$$k_a^{os} = j^* N_{Av} \sum_{i=1}^{N_S} \oiint \bar{\boldsymbol{j}}(\boldsymbol{r}) \boldsymbol{n}_i(\boldsymbol{r}) \mathrm{d}A_i^{os} / c_M^* \qquad [\mathrm{m^3\ mol^{-1}\ s^{-1}}] \qquad (26)$$

where k_a^{os} is here expressed *per particle* and per mole of reactive sites, $\bar{\boldsymbol{j}}(\boldsymbol{r}) = \boldsymbol{j}(\boldsymbol{r}) / j^*$ is the dimensionless local flux of $M_{aq}^{z_M}$ at position $\boldsymbol{r}$ with $j^* = -(D_p + D_M) c_M^* / r_p$, the maximum steady-state diffusive flux of $M_{aq}^{z_M}$ at the particle surface, (*cf.* eqn (18) in Section C2.1). Eqn (26) tacitly implies that D_M is identical in the intra- and extraparticulate volumes, which is correct provided that the water-content in the particle shell is sufficiently high. The steady-state flux $\bar{\boldsymbol{j}}(\boldsymbol{r})$ involved in eqn (26) derives from the local concentration of $M_{aq}^{z_M}$ at position $\boldsymbol{r}$, $c_M(\boldsymbol{r})$, according to the expression $\boldsymbol{j}(\boldsymbol{r}) = -D_M \left[\nabla c_M(\boldsymbol{r}) + z_M F c_M(\boldsymbol{r}) \nabla y(\boldsymbol{r}) \right]$ where $c_M(\boldsymbol{r})$ is defined by the steady-state, time-independent Nernst-Planck equation for coupled diffusive and conductive transport of $M_{aq}^{z_M}$ towards the charged NP.[41]

$$\nabla . \left[\nabla \bar{c}_M(\boldsymbol{r}) + z_M \bar{c}_M(\boldsymbol{r}) \nabla y(\boldsymbol{r}) \right] = 0 \qquad (27)$$

where $\nabla .$ and ∇ are the divergent and gradient operators in spherical symmetry,[42] and $\bar{c}_M(\boldsymbol{r}) = c_M(\boldsymbol{r}) / c_M^*$. The treatment basically extends Fick's law of diffusion to include the effect of the electric field. In eqn (27) $y(\boldsymbol{r})$ is the dimensionless equilibrium electrostatic potential applying at the position $\boldsymbol{r}$ and defined according to $y(\boldsymbol{r}) = F\psi(\boldsymbol{r}) / (RT)$ with $\psi(\boldsymbol{r})$ the potential, and *R*, *T* having their usual meanings. Within the time window where the extraparticulate diffusion profile of $M_{aq}^{z_M}$ is at steady-state (the intraparticulate diffusion is faster),[8] the intra- and extraparticulate ionic environments are considered at equilibrium. In such a setting, $y(\boldsymbol{r})$ is independent of time under the general conditions for the excess background electrolyte. This simplification is applicable at sufficiently low site coverage, i.e. assuming that the associated metal ions do not significantly contribute to the composition of the NP electric double layer and/or their binding to the reactive sites $S_{i=1,\ldots,N_S}$ does not modify the particle electrostatics (see section C2). If this assumption no longer holds then it becomes critical to evaluate the metal flux distribution within the particle shell and at the particle/solution interface

taking into account (i) the transient settling of the NP diffusion layer to steady-state, and, simultaneously, (ii) the relaxation of the interfacial potential distribution to its pertaining equilibrium profile. As before we continue here for the case where the NPs are dispersed in an aqueous medium containing indifferent electrolyte ions in large excess over $M_{aq}^{z_M}$ with a large excess of binding sites S_i over $M_{aq}^{z_M}$ [see Section B]. The relevant *spherical* equilibrium potential distribution $y(\boldsymbol{r})$ is then defined by the Poisson-Boltzmann equation:[43]

$$\Delta y(\boldsymbol{r}) - (\kappa r_p)^2 \sinh\left[y(\boldsymbol{r})\right] = -(\kappa r_p)^2 \bar{\rho}_{fix}(\boldsymbol{r}) \tag{28}$$

with the Laplacian operator $\Delta = d^2/dr^2 + 2r^{-1}d/dr$, the reciprocal Debye thickness $\kappa = (2F^2c^*/\varepsilon_0\varepsilon_r RT)^{1/2}$ (valid for a monovalent electrolyte), $\varepsilon_0\varepsilon_r$ the dielectric permittivity of the fluid, c^* the background electrolyte concentration, and $\bar{\rho}_{fix}(\boldsymbol{r}) = \rho_{fix}(\boldsymbol{r})/\left(2Fc^*\right)$ is the (dimensionless) spatial distribution of the density of charges within the shell given by

$$\rho_{fix}(\boldsymbol{r}) = \begin{cases} Q/\left(N_s V^{os}\right) \text{ for } \sqrt{(x-x_i)^2+(y-y_i)^2+(z-z_i)^2} \le r^{os} \\ 0 \text{ for } \sqrt{(x-x_i)^2+(y-y_i)^2+(z-z_i)^2} > r^{os} \end{cases} \tag{29}$$

where $i = 1,...,N_S$, Q denotes the overall particle charge, (x,y,z) are the Cartesian coordinates and (x_i, y_i, z_i) defines the location of the charge *i* within the shell. The reader is referred to previous work for details on the proper boundary conditions associated with eqns (27) and (28).[40]

C3.2 Limiting expressions of k_a^{os}

The following discussion assumes that inner-sphere complexation is not overall rate-limiting for M-NP association. For situations where the intraparticulate diffusion of $M_{aq}^{z_M}$ is *fast* compared to its diffusion from the bulk solution to the outer shell surface,[8] the only transport step relevant for k_a^{os} is the extraparticulate diffusion of $M_{aq}^{z_M}$. In such case the rate of extraparticulate diffusion is overall rate limiting for the association process. The associated rate constant, $k_{a,p}$, expressed *per particle*, directly follows from eqns (26) and (27) with the result (*cf.* eqn (13), Section C2.1):

$$k_{a,p} = 4\pi\left(D_p + D_M\right) r_p N_{Av} f_{el}(r_p) \qquad [m^3\ mol^{-1}\ s^{-1}] \tag{30}$$

where the quantity $f_{\mathrm{el}}(r_{\mathrm{p}}) = \left[r_{\mathrm{p}} \int_{r_{\mathrm{p}}}^{\infty} r^{-2} \exp(z_{\mathrm{M}} y(r)) \mathrm{d}r \right]^{-1}$ corrects the diffusion of $\mathrm{M}_{\mathrm{aq}}^{z_{\mathrm{M}}}$ from the bulk solution ($r \to \infty$) to the particle surface ($r = r_{\mathrm{p}}$) for the presence of the electric double layer field at the particle/solution interface.[32] For cases with attractive electrostatic forces between $\mathrm{M}_{\mathrm{aq}}^{z_{\mathrm{M}}}$ and NP, $f_{\mathrm{el}}(r_{\mathrm{p}})$ exceeds unity to an extent that depends on electrolyte concentration, particle size, particle surface potential and z_{M}.[32] Starting from eqn (30), the rate constant for outer-sphere $\mathrm{M}_{\mathrm{aq}}^{z_{\mathrm{M}}} \bullet \mathrm{S}_i$ association simply follows from the fraction of the incoming flux of $\mathrm{M}_{\mathrm{aq}}^{z_{\mathrm{M}}}$ that arrives at a given metal binding site S_i. This fraction is determined by a probabilistic M partitioning function P_{site}^{i}, which leads to the conversion of $k_{\mathrm{a,p}}$ for the entire particle into a $k_{\mathrm{a}}^{\mathrm{os}}$ for an individual site according to $k_{\mathrm{a}}^{\mathrm{os}} = k_{\mathrm{a,p}} \sum_{i=1}^{N_{\mathrm{s}}} P_{\mathrm{site}}^{i} / N_{\mathrm{S}}$ while formulation of $k_{\mathrm{a}}^{\mathrm{os}}$ per particle simply reads $k_{\mathrm{a}}^{\mathrm{os}} = k_{\mathrm{a,p}} \sum_{i=1}^{N_{\mathrm{s}}} P_{\mathrm{site}}^{i}$ Accounting for the difference between the potential experienced by the intraparticulate free $\mathrm{M}_{\mathrm{aq}}^{z_{\mathrm{M}}}$ and the potential applying at the location of the metal binding site $\mathrm{S}_{i=1,\ldots,N_{\mathrm{S}}}$, $k_{\mathrm{a}}^{\mathrm{os}}$ (per site) is then defined by

$$k_{\mathrm{a}}^{\mathrm{os}} = 4\pi \left(D_{\mathrm{p}} + D_{\mathrm{M}} \right) r_{\mathrm{p}} N_{\mathrm{a}} f_{\mathrm{el}}(r_{\mathrm{p}}) \frac{\sum_{i=1}^{N_{\mathrm{s}}} \iiint_{V^{\mathrm{os}}} \exp(-z_{\mathrm{M}} y(\boldsymbol{r})) \mathrm{d}\boldsymbol{r} \; / \; N_{\mathrm{s}}}{\sum_{i=1}^{N_{\mathrm{s}}} \iiint_{V^{\mathrm{os}}} \exp(-z_{\mathrm{M}} y(\boldsymbol{r})) \mathrm{d}\boldsymbol{r}_{\mathrm{s}} + \iiint_{V_{\mathrm{shell}} - N_{\mathrm{s}} V^{\mathrm{os}}} \exp(-z_{\mathrm{M}} y(\boldsymbol{r})) \mathrm{d}\boldsymbol{r}} \qquad [\mathrm{m^3\ mol^{-1}\ s^{-1}}] \qquad (31)$$

where integration is performed either over the volume V^{os} of the site $\mathrm{S}_{i=1,\ldots,N_{\mathrm{S}}}$ or over the volume $V_{\mathrm{shell}} - N_{\mathrm{S}} V^{\mathrm{os}}$ with V_{shell} the shell volume. In situations where the outer-sphere volume of $\mathrm{S}_{i=1,\ldots,N_{\mathrm{S}}}$ and the remaining shell volume are at the same potential - which is applicable within the Donnan regime valid for $(r_{\mathrm{p}} - a) >> \kappa^{-1}$ (with *a* the radius of the NP core component, if any) and for systems with sufficiently high charge density - eqn (31) simply reduces to:[40]

$$k_{\mathrm{a}}^{\mathrm{os}} = 4\pi \left(D_{\mathrm{p}} + D_{\mathrm{M}} \right) r_{\mathrm{p}} N_{\mathrm{Av}} f_{\mathrm{el}}(r_{\mathrm{p}}) \frac{V^{\mathrm{os}}}{V_{\mathrm{shell}}} \qquad [\mathrm{m^3\ mol^{-1}\ s^{-1}}] \qquad (32)$$

In the other extreme where the density of particle charges is so low that the non-zero potential condition only applies in the direct vicinity of $S_{i=1,\ldots,N_S}$, eqn (31) becomes (*cf.* the potential profile for the classical individual site limit; Fig. 3(b)):

$$k_a^{os} = 4\pi\left(D_p + D_M\right) r_p N_{Av} f_{el}(r_p) \frac{\iiint_{V^{os}} \exp(-z_M y(\boldsymbol{r}))\mathrm{d}\boldsymbol{r}}{N_s V^{os}\left[\iiint_{V^{os}} \exp(-z_M y(\boldsymbol{r}))\mathrm{d}\boldsymbol{r} / V^{os} - 1\right] + V_{shell}}. \qquad [\mathrm{m^3\ mol^{-1}\ s^{-1}}] \qquad (33)$$

The limiting expressions (32) and (33) satisfactorily compare with the results given in previous work[9] for k_a^{os} expressed on a per site basis.

C3.3 Implications of discretisation for the magnitude of reactivity descriptors

For a given spatial distribution of charged metal binding sites $S_{i=1,\ldots,N_S}$, the potential distribution $y(\boldsymbol{r})$ is evaluated from numerical solution of eqn (28)[40] and k_a^{os} is subsequently estimated from the general expression, eqn (26), or from the approximate eqns (32) and (33) relevant in the high and low charge density regimes with neglect of inner particulate $M_{aq}^{z_M}$ concentration gradients, respectively. Fig. 4 shows the typical intraparticulate distributions of the electrostatic potential at different levels of particle charge screening (represented by the dimensionless quantity κr_p), and for different number N_S of charged metal binding sites randomly distributed throughout the fully porous particle ($a \to 0, V_{shell} \to V_p$). Intraparticulate potential gradients gradually vanish upon (i) increasing N_S, *i.e.* with increasing NP charge density, and/or (ii) decreasing κr_p, *i.e.* with decreasing electrolyte concentration and/or particle radius. In both cases, the overlap between the ionic environments of adjacent S_i becomes significant, and the resulting potential profile satisfactorily merges with that evaluated on the basis of eqn (28) where the density of particle charges is smeared-out over the entire particle shell volume (Fig. 4), *i.e.* $\rho_{fix}(\boldsymbol{r}) \to Q / V_{shell}$.

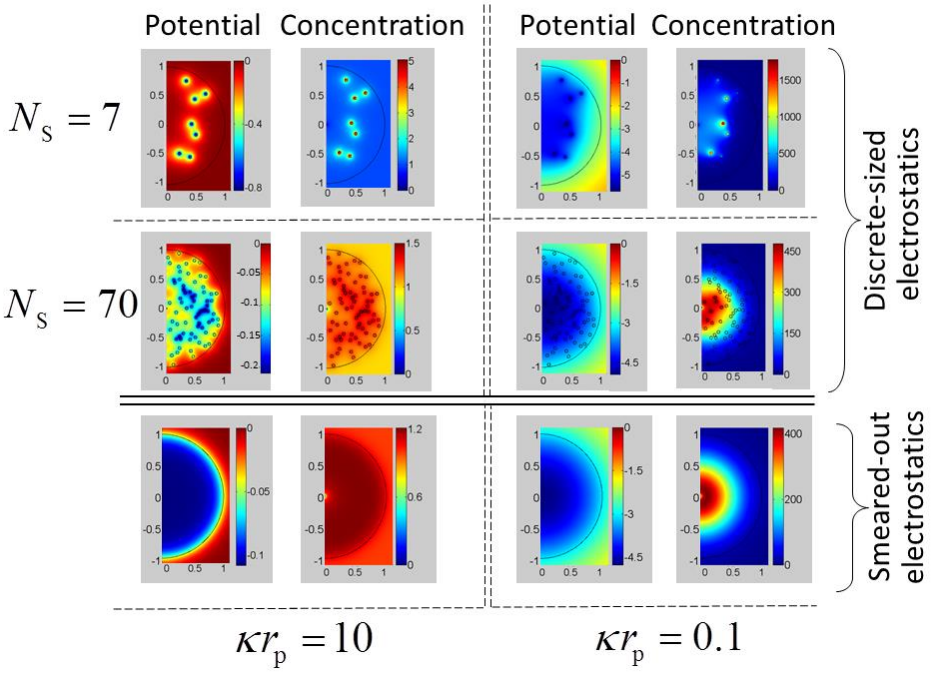

Fig. 4 Typical intraparticulate distributions for the electrostatic potential and metal concentration for the various indicated values of N_S and κr_p . $Q = -100|e|$ (with *e* the elementary charge), $a \to 0$, $z_M = 2$, $r_p = 20\,\text{nm}$, $D_M = 10^{-9}\ \text{m}^2\ \text{s}^{-1}$ ($>> D_p$). The reported spatial and concentration variables are normalized by r_p and c_M^*, respectively, and the (dimensionless) potential is given in terms of $y(\boldsymbol{r})$. Results are given for discrete electrostatics (top 8 panels in the figure) and smeared-out electrostatics (bottom 2 panels, $N_S = 70$). Redrawn from Fig. 5 in ref. 40.

Figure 5 shows the effects of the particle electrostatic field on the rate constant k_a^{os} (eqn (26)) for outer-sphere M-NP formation. Regardless of the way in which the electrostatic field is treated, *i.e. via* a discrete or a smeared-out approach, k_a^{os} increases with increasing N_S and/or decreasing κr_p as a result of the corresponding enhancement of the electrostatically-driven acceleration (f_{el}) of the diffusion of M^{2+} towards the negative particle surface. Under the conditions of Fig. 5, this increase in k_a^{os} is slightly more pronounced within the framework of the discrete electrostatic approach as compared to that evaluated from eqn (28) with smeared-out particle charge. In this latter case, the influence of the individual particle charges is effectively diluted, resulting in a decrease in magnitude of the particle surface potential (see Fig. 4). Consequently, the conductive acceleration of M towards $S_{i=1,\ldots,N_S}$ is reduced, which in turn lowers k_a^{os}. With decreasing N_S, the

particle charge $Q = -2|e|N_S$ decreases: this basic feature explains the convergence of the k_a^{os} values to the same asymptotic (non-conductive) diffusion-controlled regime, irrespective of κr_p (Fig. 5). Furthermore, eqn (33) valid for k_a^{os} in the low-charge density limit, very well reproduces the numerical results obtained at κr_p = 10. This is so because under conditions where the steady-state NP diffusion layer thickness δ_{NP} ($\sim r_p$) is much greater then $1/\kappa$,[43,44] the intraparticulate concentration gradient resulting from intraparticulate diffusion of $M_{aq}^{z_M}$ does not play any significant role in determining the partitioning of $M_{aq}^{z_M}$ between the metal binding sites' location and the remaining particle volume. This argument is further confirmed upon inspection of the metal concentration profiles evaluated at κr_p = 10 with smeared-out and discrete electrostatics (Fig. 4).

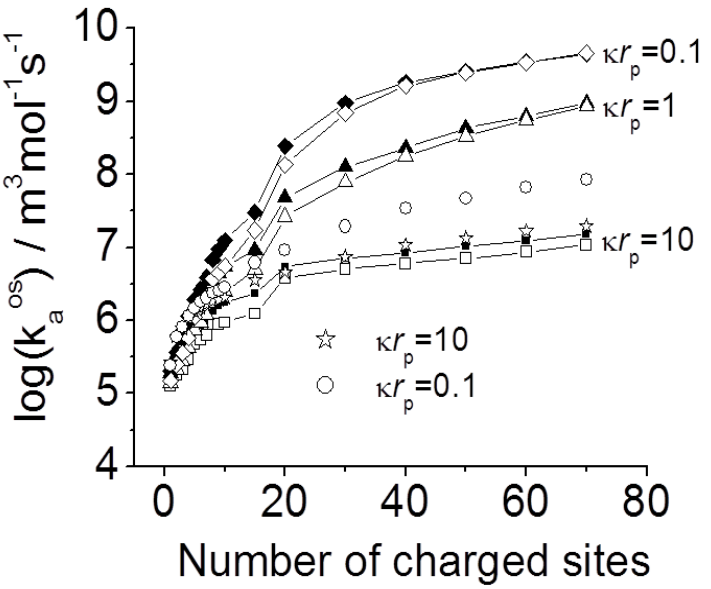

Fig. 5 Dependence of k_a^{os} (expressed on a per particle basis) on the number N_s of charged metal binding sites for different values of electrolyte concentrations or equivalently κr_p ($r_p = 20$ nm). Open and solid symbols connected by solid lines correspond to evaluations from eqn (26) with smeared-out and discrete electrostatics, respectively. Predictions from eqn (32) for κr_p = 0.1 are shown as open circles, and predictions from eqn (33) for $\kappa r_p = 10$ are shown as open stars. Calculations were carried out for a porous particle with a randomly generated uniform distribution. $Q = -2|e|N_S$ and $D_M = 10^{-9}$ m^2 s^{-1} $(>> D_p)$. Redrawn from Fig. 3 in ref. 40.

As the magnitude of the intraparticulate electrostatic field increases, significant deviations are observed between the predictions from eqn (26) and eqn (32) relevant for equipotential particulate volume. The observed

discrepancy stems from the significant gradient in the intraparticulate concentration of $M_{aq}^{z_M}$ (see Fig. 4). This factor is ignored in the derivation of eqn (32), but it becomes significant when $\delta_{NP} << 1/\kappa$, i.e. at sufficiently low κr_p (Fig. 4). In line with this reasoning, deviations between k_a^{os} computed via eqn (26) and eqn (32) at low κr_p gradually disappear upon switching from a particle volume to a particle surface distribution of metal binding sites, *i.e.* from soft to hard NPs.[40] As a last illustration of this section, Fig. 6 shows how the intraparticulate metal binding site distribution affects k_a^{os}. Results are shown at $\kappa r_p = 1$ as a function of N_S for random and non-uniform distributions of $S_{i=1,...,N_S}$ (see inset, Fig. 6) and for a particle size $r_p = 20$ nm. For the sake of comparison, the particle charge $Q = -100|e|$ is fixed independently of N_S and each site thus carries a charge Q / N_S. At sufficiently large N_S, the discrete and smeared-out electrostatic approaches lead to similar k_a^{os} values (not shown) for the reasons already detailed above. Convergence between the two data sets is also attained at lower N_S upon decreasing the distribution-dependent characteristic length scale $< \ell_S >$ relative to the average site-to-site separation distance, *i.e.* when the latter becomes much lower than the Debye layer thickness $1/\kappa$, which confirms the validity of the smeared-out electrostatic approach. At fixed N_S, Fig. 6 demonstrates that the k_a^{os} pertaining to a uniform site distribution is lower than that for a non-uniform repartition of $S_{i=1,...,N_S}$. In the latter situation, the conductive acceleration of metal diffusion to $S_{i=1,...,N_S}$ is indeed favored because the overall particle charge *Q* is confined within an effective sphere of radius less than r_p (see inset). This setting leads to enhancement of the extent to which the intraparticulate $M_{aq}^{z_M}$ is electrostatically partitioned between the reactive outer-sphere volume and the remainder of the particle body. At sufficiently low N_S, the distinction between non-uniform and uniform site distributions becomes immaterial, i.e. once $\kappa \ell_S >> 1$ and only a few highly-charged metal binding sites are carried by the particle. The distribution of Q over such a restricted number of sites consequently generates potentials that are operational only at the site locations. These potentials are so large (in magnitude) that they lead to a significant increase in k_a^{os} as compared to those obtained at larger N_S where the particle charge *Q* is 'diluted' over larger intraparticulate volumes.

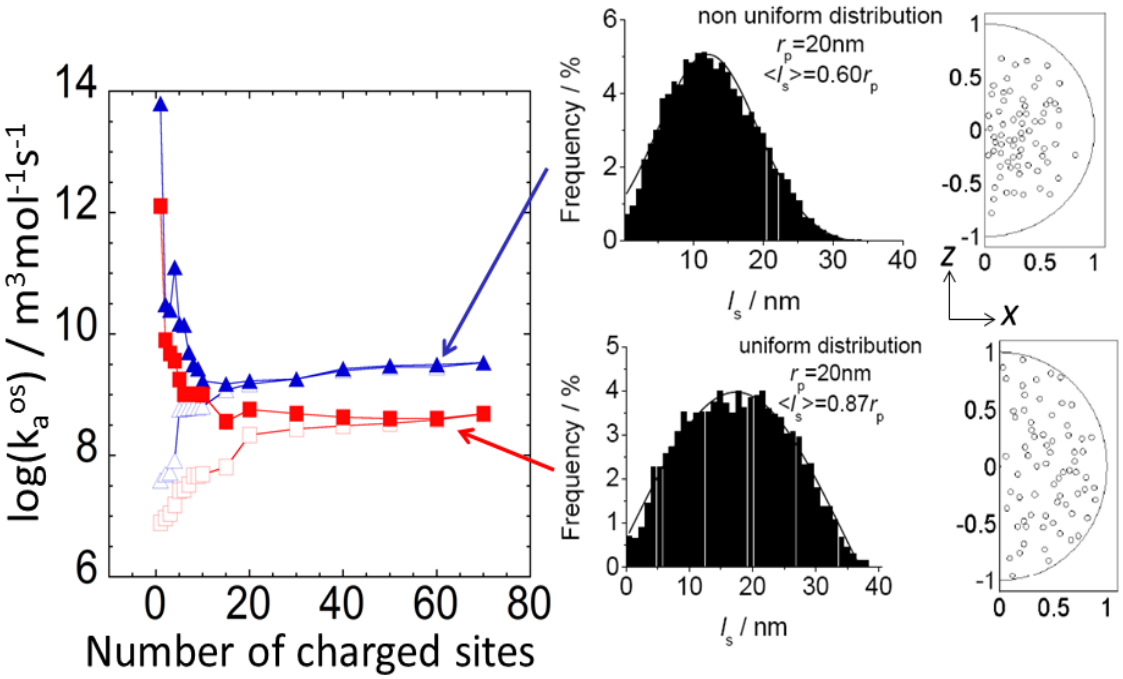

Fig. 6 Effect of the intraparticulate metal binding site distribution on k_a^{os} (expressed on a per particle basis), eqn (26), with discrete (solid symbols) and smeared-out (open symbols) electrostatics. Red and blue symbols correspond to simulations performed with adopting uniform and non-uniform distributions (see inset) generated with a site density probability function in the specified (x,z) plane set to $1/\pi$ and $6\left(1-\sqrt{(x/r_p)^2+(z/r_p)^2}\right)^2/\pi$, respectively. $D_M = 10^{-9}$ m^2 s^{-1} $(>> D_p)$, $r_p = 20$ nm, $Q = -100|e|$, $\kappa r_p = 1$. The average site-to-site separation distance $<\ell_S>$ associated with the tested site distributions is further specified for $N_S = 70$. Redrawn from results presented in ref. 40.

C4 Analytical expressions for limiting cases in the overall complexation reaction

The rate constant expressions for straightforward limiting cases in which the overall rate of association / dissociation is either limited by (i) diffusive supply of free M^{2+} towards / from the NP, or (ii) formation / dissociation of the inner-sphere complex are given in Sections C2 and C1 respectively. The rate-limiting step for association is determined by the relative magnitude of the rate of diffusive supply of M_{aq}^{2+} towards the NP and the rate of inner-sphere complex formation *within* the particle. The rate constant (per site) for the overall association reaction, k_a, can be expressed in a composite form which inherently accounts for intermediate cases in which diffusion to the particle and inner-sphere complex formation occur on comparable timescales,[45] i.e.:

$$k_a = (1/k_{a,p} + 1/k_a^{is})^{-1} \qquad [m^3\ mol^{-1}\ s^{-1}] \qquad (34)$$

However, eqn 34 is only applicable if each of the rate constants are to be multiplied by the same metal ion and reactive site concentrations in the corresponding rate expressions. Accordingly, the appropriate comparison requires multiplying the expression for k_a^{is}, eqn 7, by $\overline{f}_B$ (see Section C5 for details). Figure 7 shows how the association rate constants depend on the particle size and metal dehydration rate for soft (Fig. 7(a)) and hard (Fig. 7(b)) particles in the high charge density regime. As k_w increases, the association rate is increasingly limited by diffusion towards the particle surface and thus $k_{a,p}$ progressively becomes the predominant contributor to k_a. The plateau regions in Fig. 7 are attained when k_a approaches $k_{a,p}$ and the association process has become essentially independent of k_w. The k_w value at which $k_a \approx k_{a,p}$, decreases with increasing r_p and increasing $\overline{f}_B$.

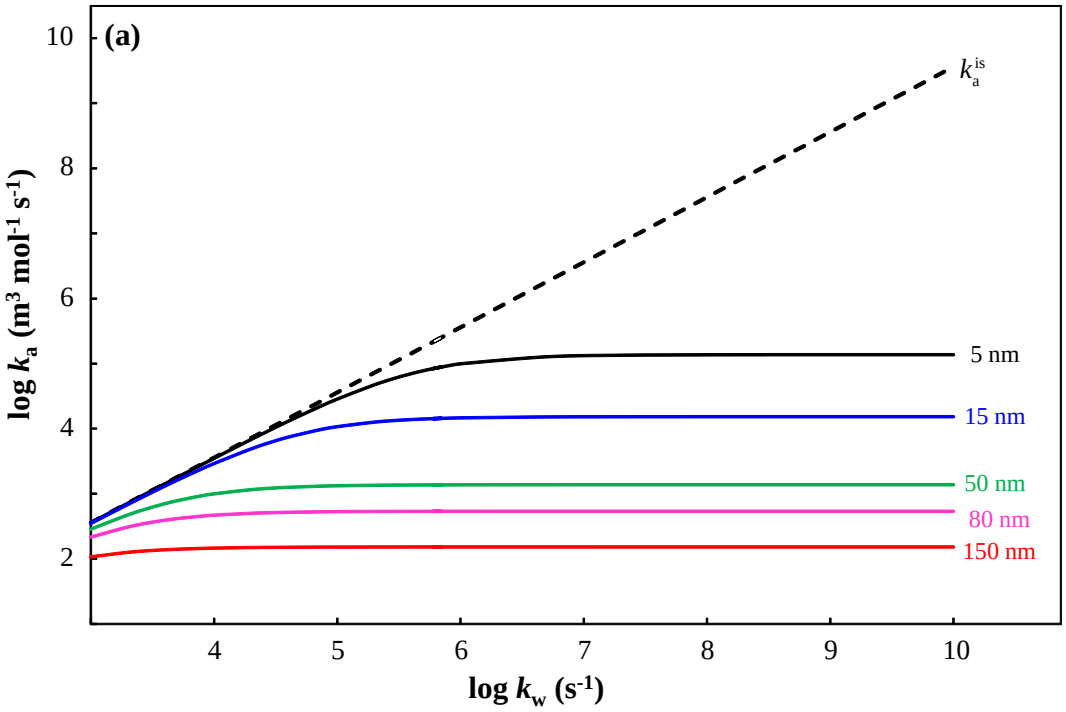

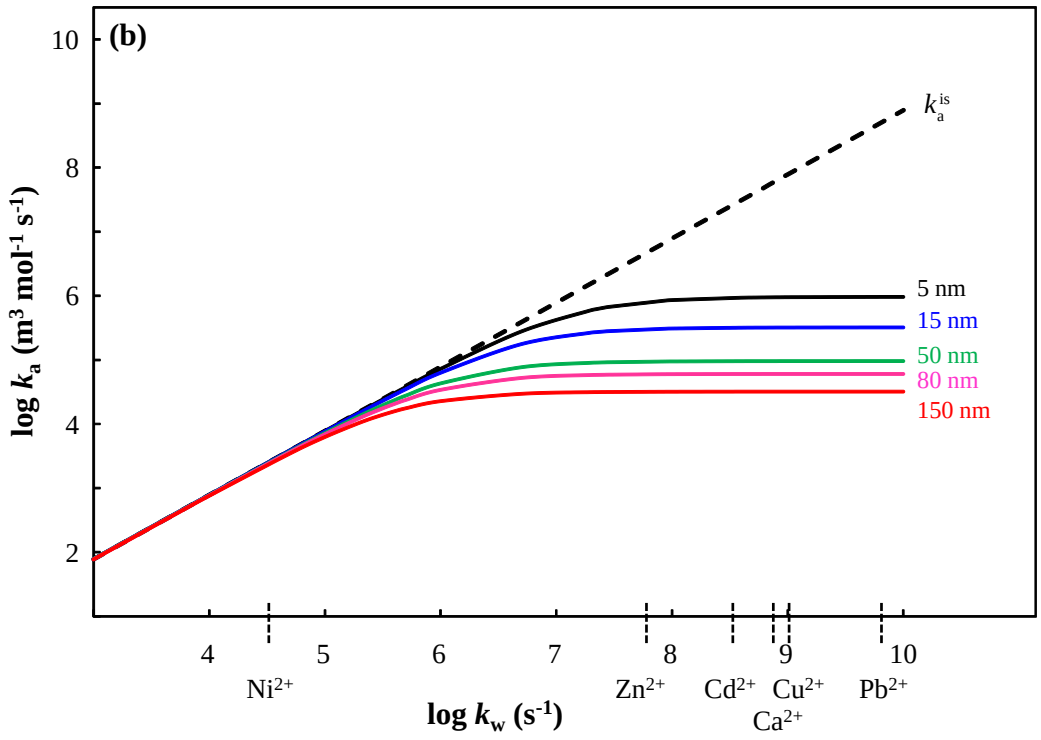

Fig. 7 Comparison of the rate constant for inner-sphere complex formation, k_a^{is} (dashed black line) with the overall association rate constant, k_a (solid curves), for a range of (a) soft, 3D and (b) hard, 2D particle radii as a function of the metal dehydration rate constant, k_w. The k_w values for selected metal ions are indicated on the *x*-axis. The various r_p values are indicated on the figure; the magnitude of k_a^{is} is independent of r_p. Computations are performed for: 3D c_S = 700 mol m^{-3}, 2D Γ_S = 1.7x 10^{-7} mol m^{-2}, D_M = 8x10^{-10} m^2 s^{-1},[46] $\overline{f}_B$ = 500.

Analogously, since the limiting rates of dissociation are governed by the concentration of intraparticulate M_{aq}^{2+}, the composite rate constant for dissociation, k_d, can be written as:

$$k_d = (1/k_{d,p} + 1/k_d^{is})^{-1} \qquad [s^{-1}] \qquad (35)$$

Now, in addition to the effect of r_p and k_w, the overall rate of dissociation is also influenced by the magnitude of the intrinsic affinity constant, K_{int}, via its impact on both $k_{d,p}$ (eqs 16 and 17) and k_d^{is} (eqs 9 and 12). Figure 8 shows how the dissociation rate constants depend on the particle size and metal dehydration rate for soft and hard particles in the high charge density regime. In comparison to the association step (Fig. 7), the effect of particle size on the dissociation rate constants is moderated by the magnitude of K_{int}, whilst we also see that as

k_w increases, the dissociation rate becomes increasingly limited by diffusion from the particle surface to the bulk medium and thus $k_{d,p}$ progressively becomes the predominant contributor to k_d.

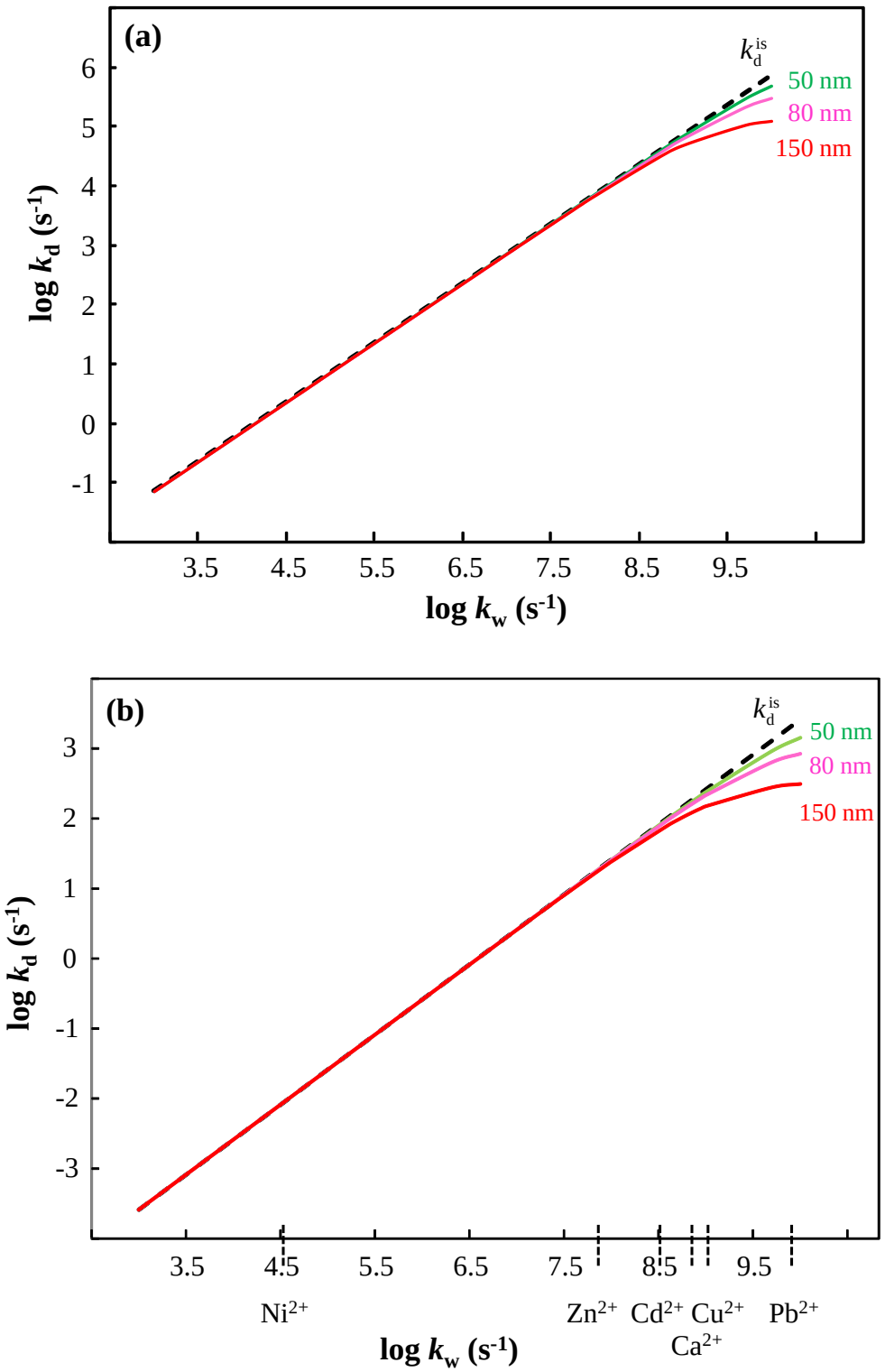

Fig. 8 Comparison of the rate constant for dissociation of the inner-sphere complex, k_d^{is} (dashed black line) with the overall dissociation rate constant, k_d (solid curves), for a range of (a) soft, 3D and (b) hard, 2D particle

radii as a function of the metal dehydration rate constant, $k_{w.}$ The k_w values for selected metal ions are indicated on the *x*-axis. For r_p values of 5 and 15 nm, k_d is practically equal to k_d^{is} over the entire k_w range shown; the magnitude of k_d^{is} is independent of r_p. Computations are performed for: 3D: K_{int} = 10 m^3 mol^{-1}, c_S = 700 mol m^{-3}; 2D: K_{int} = 10^6 m^3 mol^{-1}, K_H = 1x10^{-4} m, Γ_S = 1.7x10^{-7} mol m^{-2}; D_M = 8x10^{-10} m^2 s^{-1}.[46]

Depending on the chemodynamic features of a given NP system, a change in e.g. ionic strength can change which step in the overall process of association or dissociation is rate limiting, i.e. diffusive supply/efflux or inner-sphere complex formation/dissociation (see the example given in Section D2.2).

C5 Lability concepts for NP complexes

The concept of lability refers to the extent to which metal complexes dissociate and release the free metal ion on the timescale of their diffusion towards a reactive surface, e.g. a sensor or an organism that accumulates the free ion. The setting is shown in Fig. 9, from which it is evident that the chemodynamics of dispersed nanoparticulate complexes are involved with the frequency of exchange of M between M_{aq}^{2+} in the *bulk* dispersion medium and MS within the particle body. Accordingly, for description of processes at the macroscopic level, the rate expressions must be formulated in terms of concentrations averaged over the entire volume of the dispersion (*cf.* the intraparticulate processes in the preceding sections). Since $c_M = \overline{f}_B\, c_M^*$, it simply means that the expression for k_a^{is} (*cf.* eqn (7)) becomes:

$$k_a^{is} = k_w V^{os} N_{Av} \overline{f}_B \qquad [m^3\ mol^{-1}\ s^{-1}] \qquad (36)$$

The chemodynamic features of metal complexes are defined at two levels.[47] Firstly, a system is denoted as *dynamic* in terms of a conventional volume complexation reaction, if there is frequent interchange between free M_{aq}^{2+} in the bulk medium and MS on the timescale of interest, *t*, i.e.:

$$k_a \bar{c}_S t >> 1 \quad \text{and} \quad k_d t >> 1 \qquad (37)$$

where the applicable k_a and k_d are the composite rate constants for the overall association and dissociation processes (with k_a^{is} given by eqn (36)) and $\bar{c}_S$ is the concentration of sites averaged over the dispersion

volume. At the other extreme, an *inert* system will not significantly re-equilibrate in response to a change in species concentrations in the surrounding aqueous medium, i.e.

$$k_a \bar{c}_S t \ll 1 \quad \text{and} \quad k_d t \ll 1 \tag{38}$$

Then, in the context of an ongoing process at a reactive surface, e.g. conversion and removal of free M_{aq}^{2+} from the dispersion, the ability of the system to maintain the $M_{aq}^{2+} + S \leftrightarrow MS$ complexation equilibrium is described by the concept of lability. In this regard the approximative Koutecký-Koryta (KK) scheme,[10,48-50] has shown great utility for describing the lability of molecular complexes,[51-53] and has recently been adapted to the case of nanoparticulate metal complexes.[14] The KK approximation divides the concentration profiles of free and complexed M in the diffusion layer into a labile and a nonlabile region, separated by the boundary of the reaction layer, i.e. at a distance λ from the macroscopic interface. In the case of nanoparticulate complexants, distinction has to be made between (i) a conventional *intraparticulate* reaction layer, with thickness λ_{NP}, at the particle side of the NP/medium interface,[13] and (ii) an operational reaction layer, $\bar{\lambda}$, that is effective at the surface of a macroscopic reacting/sensing interface (Fig. 9).[14] In the NP case, the operational reaction layer is related to the time-averaged presence of particle body volume and its corresponding time-averaged complexing site concentration, $\bar{c}_S^{\lambda}$. On this basis, and assuming no interactions between the M-NP entity and the sensing interface, $\bar{\lambda}$ derives from the mobility of free M_{aq}^{2+} in the aqueous dispersion, D_M , and its mean free lifetime $1/k_{a,p}\bar{c}_S^{\lambda}$, as well as the mobility of the complex MS ($\approx D_p$) and its mean free lifetime ($1/k_d$):

$$\bar{\lambda} = \left(\frac{k_{a,p}\bar{c}_S^{\lambda}}{D_M} + \frac{k_d}{D_p} \right)^{-1/2} \quad [\text{m}] \tag{39}$$

where k_d is the composite dissociative rate constant (eqn 35). The value of $\bar{c}_S^{\lambda}$ is obtained by an iterative procedure,[14] and is evidently immaterial if the magnitude of $\bar{\lambda}$ is governed by the dissociative term in eqn (39). The associative component in eqn (39) contains only $k_{a,p}$ and not the composite k_a (intraparticulate diffusion of free M_{aq}^{2+} fast, *cf.* previous work[14]). The approach implies that when $\bar{\lambda}$ has the same order of magnitude as r_p , an NP body *volume exclusion* effect will come into effect.[14,54]

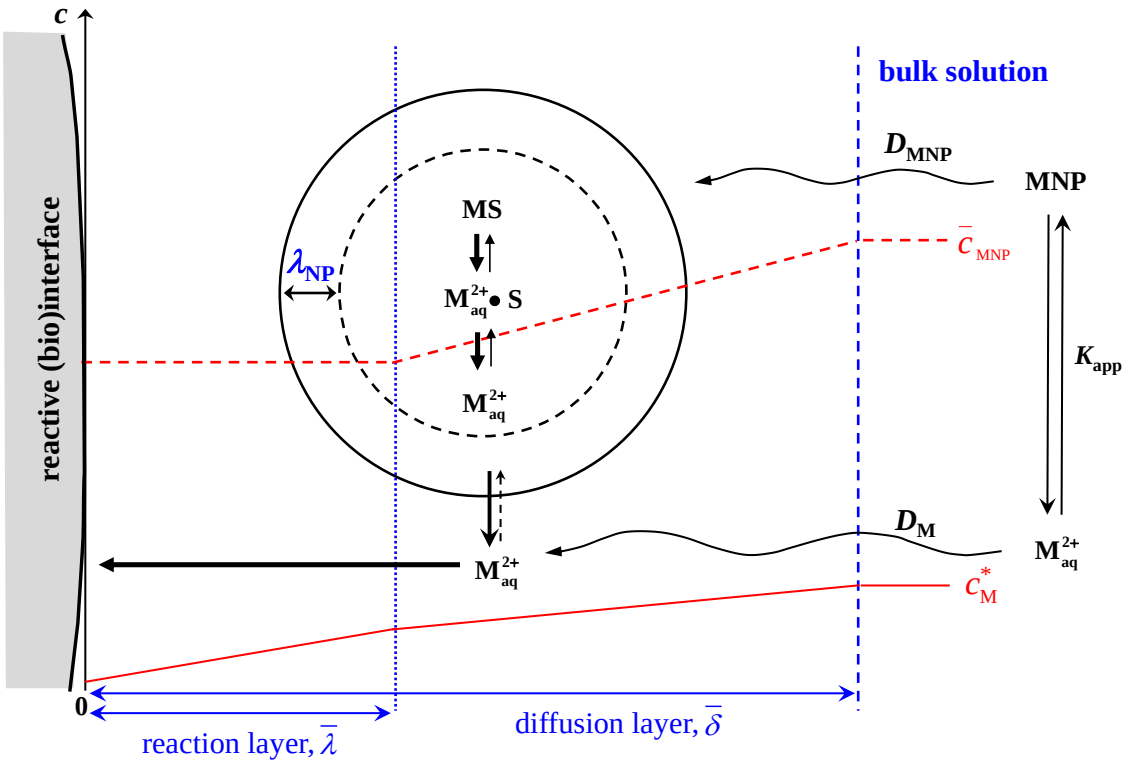

Fig. 9 Schematic view of the various processes governing the flux of M towards a macroscopic interface (e.g. a sensor or an organism) that reacts with free M^{2+}_{aq}, in an aqueous dispersion of nanoparticulate complexes of M. The concentration profile of the free M^{2+}_{aq} in the medium, c^*_M, is sketched by the solid red line, and the profile of the average concentration of MS complexes within each spatial zone, $\bar{c}_{MS}$, is indicated by the dashed red line. For clarity, the size of the NP is exaggerated and arbitrary thicknesses are shown for the intraparticulate reaction layer, λ_{NP}, the operational reaction layer at the macroscopic interface, $\bar{\lambda}$, and the mean solution diffusion layer for M^{2+}_{aq} and MS, $\bar{\delta}$. Figure is adapted from Fig. 2 in ref. 14.

The so-called lability parameter for nanoparticulate MS, $\mathcal{L}_{NP}$, is defined in the same general manner as for molecular ligands,[55,56] i.e. as the ratio between the kinetic and diffusive fluxes. The kinetic flux J_{kin}, represents the rate of release of M^{2+}_{aq} from the particle body. Since the diffusion-controlled release of M^{2+}_{aq} into the bulk medium (local diffusion shell with thickness r_p) can be considered to be fast compared to the macrodiffusion process, only the rate of chemical dissociation of MS is relevant for J_{kin}, i.e:

$$J_{\text{kin}} = k_{\text{d}}^{\text{is}} \bar{c}_{\text{MS}}^{\lambda} \bar{\lambda} \qquad [\text{mol m}^{-2}\ \text{s}^{-1}] \qquad (40)$$

where $\bar{c}_{\text{MS}}^{\lambda}$ is the average concentration of MS within the macroscopic reaction layer zone.

The limiting purely diffusive flux of the complex M-NP system, J_{dif}^{*}, represents the rate at which *all forms* of M present in the dispersion arrive at the macroscopic interface, i.e. the free $\text{M}_{\text{aq}}^{2+}$ in the bulk dispersion, as well as the various intraparticulate forms, comprising the free $\text{M}_{\text{aq}}^{2+}$, the inner-sphere complex MS (labile in the limiting flux), and any other relevant species, e.g. electrically condensed M^{2+} ions. The ensuing expression for J_{dif}^{*} is given by:

$$J_{\text{dif}}^{*} = \bar{D}(c_{\text{M}}^{*} + \bar{c}_{\text{MS}} + \bar{c}_{\text{M}} + ...) / (1/\bar{\delta} + 1/r_0)^{-1} \qquad [\text{mol m}^{-2}\ \text{s}^{-1}] \qquad (41)$$

where the overbar on the concentration terms denotes the intraparticulate forms of M expressed as smeared-out averages over the dispersion, r_0 is the radius of the sensing (bio)surface, $\bar{\delta}$ is the mean diffusion layer thickness as determined by the hydrodynamic flow conditions at the reactive interface,[57] and $\bar{D}$ is the mean diffusion coefficient for the complex system:

$$\bar{D} = \frac{D_{\text{M}} c_{\text{M}}^{*} + D_{\text{p}}(\bar{c}_{\text{MS}} + \bar{c}_{\text{M}} + ...)}{\bar{c}_{\text{M,t}}} \qquad [\text{m}^2\ \text{s}^{-1}] \qquad (42)$$

where $\bar{c}_{\text{M,t}}$ is the total metal concentration averaged over the entire dispersion. As compared to the scale of the nanoparticle, a microscale interface is relatively 'macroscopic': when $r_0 >> \bar{\delta}$, the spherical term in eqn 41 with $1/r_0$ disappears, whereas for a microscale interface with $r_0 << \bar{\delta}$, the radial diffusive terms governs the flux.

The lability parameter, $\mathcal{L}_{\text{NP}}$, follows as:

$$\mathcal{L}_{\text{NP}} = J_{\text{kin}} / J_{\text{dif}}^{*} = k_{\text{d}}^{\text{is}} \bar{c}_{\text{MS}}^{\lambda} \bar{\lambda} / \left(\bar{D}(c_{\text{M}}^{*} + \bar{c}_{\text{MS}} + \bar{c}_{\text{M}} + ...) / (1/\bar{\delta} + 1/r_0)^{-1} \right) \qquad (43)$$

A system is denoted as *labile* if $\text{M}_{\text{aq}}^{2+}$ + S ↔ MS complexation equilibrium is maintained at any relevant scale so that there is coupled diffusion of the free and complex species of the target ion. In this case the flux of $\text{M}_{\text{aq}}^{2+}$

from the NP body towards the reactive interface is a purely diffusion-limited one. If, on the other hand, such equilibrium cannot be maintained to an appreciable extent, the system is *nonlabile* and the metal flux is kinetically controlled by the rate of dissociation of the complex.

D. Illustrative experimental evidence and discussion

Application of the conceptual framework to the interpretation of experimental data on nanoparticulate metal complexes requires knowledge of the NP's characteristics such as size, charge density, and permeability. Various techniques are available to determine the size of NPs in aqueous dispersions, including dynamic light scattering,[58,59] fluorescence correlation spectroscopy,[60-62] nanoparticle tracking analysis,[63,64] and flow field-flow fractionation.[65,66] Each approach has certain limitations, e.g. constraints on the NP shape and the relative weighting of size fractions in heterogeneous samples.[65,67-69] The descriptors for the particle electric field can be estimated by electrokinetic techniques, e.g. electrophoresis. In recent years, advanced models have been developed for adequate interpretation of electrokinetic properties of soft nanoparticles.[70,71] The interpretation framework enables the volume charge density, hydrodynamic properties and diffuse nature of the soft charged particle/medium interface to be obtained from electrophoretic mobility data.

It is evident from the preceding sections that the chemodynamic features of an M-NP system depend on the properties of both the metal ion and the NP; the accessible range of parameters is also determined by the operational timescale of the analytical technique employed (*cf.* eqn (43)). A suite of dynamic analytical techniques for measuring the fluxes and reactivities of metal complexes over a range of operational timescales are available, including various voltammetric methods,[72] diffusive gradients in thin film (DGT),[73,74] as well as dynamic modes of permeation liquid membrane (PLM)[56,75,76] and Donnan membrane techniques (DMT).[77,78] The principles of operation of these techniques have been critically reviewed,[55] and their typical responses placed in context of the chemodynamic features of soft nanoparticulate metal complexes.[79] The electrochemical technique of stripping chronopotentiometry at scanned deposition potential (SSCP),[80,81] has emerged as a particularly powerful tool for obtaining robust parameters to describe metal binding by nanoparticles. An SSCP wave is constructed from measurements of target metal reoxidation time as a function of the reduction potential in the preceding accumulation step: the response from the foot of the wave to the

limiting deposition current plateau successively probes the free metal ion concentration and progressively a window of the stability and rate constant distributions. As a consequence, chemical heterogeneity in the metal complexation leads to a flattening of the SSCP wave; the nature of the technique implies that such effects can be unambiguously distinguished from those of electrochemical irreversibility.[82-84] It is fruitful to combine the dynamic information from SSCP waves with determination of the free metal ion concentration by the so-called AGNES technique (absence of gradients and Nernstian equilibrium stripping).[85] AGNES exploits attainment of equilibrium in the foot of the SSCP wave to determine the free metal ion concentration in the bulk aqueous medium. The implementation of SSCP with conventional electrodes and microelectrodes covers a useful operational timescale for many practical M-NP systems. The analytical signal in the plateau region (representing the limiting deposition current) for the metal ion in the presence and absence of the NP complexant gives a direct measure of the lability of the M-NP species.[79,86] It is worth noting that the larger the NP, the lower is its diffusion coefficient, and thus the smaller is the diffusive flux of its metal complexes, eqn (41), and the greater is their lability, eqn (43). Accordingly, the sensitivity of a given analytical technique determines the window of accessible chemodynamic parameters, together with other practical characteristics e.g. the time required to attain a steady-state flux in DGT.[87] The following sections highlight selected experimental results that illustrate the applicability of the developed conceptual framework for various types of M-NP systems.

D1. Hard nanoparticles

Hard nanoparticles that form complexes with metal ions typically contain functional groups on their surface. They are thus often effectively core-shell particles, albeit that the shell thickness is of the order of a nm.[88] A wide variety of engineered NPs fall in this category, e.g. functionalized latex[89] and silica[90], as well as metallic NPs that are often surface-coated to enhance their handling properties.[91-93] Cd(II) complexes with carboxyl-functionalized latex NPs have been found to be partially labile by differential pulse polarography.[1] Figure 10 compares the measured voltammetric current (solid black points), with that predicted for the fully labile case (black dashed line) and that computed by accounting for the lability of the nanoparticulate complexes, (blue dashed line), i.e. the product of the lability parameter, eqn (43), and the fully labile case. The outcome highlights the significance of volume exclusion from the macroscopic reaction layer (eqn (39)). For the given

conditions the NP body volume fraction in the reaction layer $\bar{\lambda}$ is 3.5% of that in the bulk medium;[54] if the exclusion factor would be ignored, the system would be erroneously predicted to be close to the labile limit. Thus the interpretation of the experimental data in light of the new modelling framework presented above reveals a remarkably good agreement between experiment and theory.

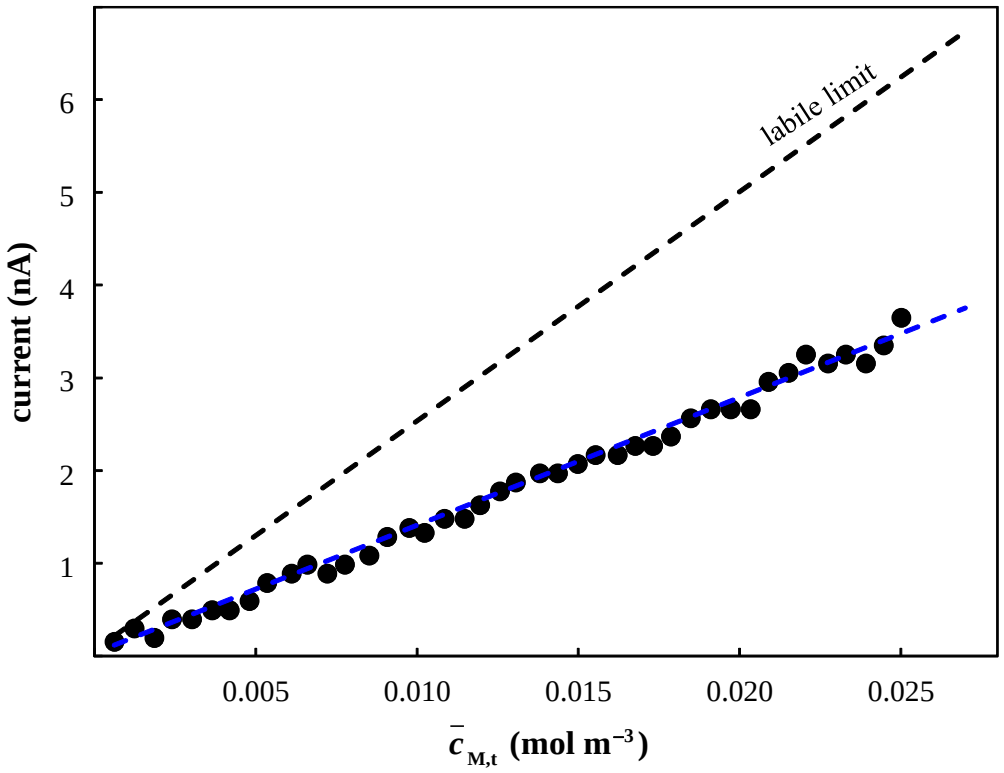

Fig. 10 Comparison of measured (points) and predicted (curves) voltammetric current for Cd(II) complexes with carboxyl-functionalized NPs. Experimental data are shown as solid black points, the current predicted for fully labile Cd(II)-NP complexes is indicated by a dashed black curve, and that predicted on the basis of the lability parameter for M-NPs (eqn 43) is shown as a blue dashed curve. Experimental conditions: pH 6.5, ionic strength 10 mol m^{-3}, $\bar{c}_S$ = 0.25 mol m^{-3}. Measurements were made using differential pulse polarography with a sampling time of 10 ms, and a static mercury drop electrode (Metrohm) as the working electrode.[1] Parameters: r_p = 71 nm,[94] shell thickness d taken as 1 nm,[88] $K_{int} = K_{app}/\bar{f}_B$ = 2.25 m^3 mol^{-1}, $\bar{f}_B$ = 140.5, $\bar{f}_{el,a}$ = 1.16, D_p = 3.09x10^{-12} m^2 s^{-1}, D_{Cd} = 7x10^{-10} m^2 s^{-1},[46] $\bar{\lambda}$ = 1x10^{-8} m, $\bar{\delta} = (\pi \bar{D} t)^{1/2}$ = 6.1x10^{-7} m.[95] Figure is adapted from Fig. 7 in ref.1.

D2. Soft nanoparticles

Humic acids (HA) are natural heterogeneous complexants that exhibit characteristics typical of soft charged nanoparticles.[96] They typically have radii in the range 5 nm to the order of 100 nm depending on their origin and aggregation state, as determined by the concentration of the dispersion, pH, ionic strength, hydrophobicity, *etc*.. Although the structural details of the individual particles are not rigorously known, there is a large body of literature on their metal binding properties. The inherent heterogeneity of HA makes rigorous interpretations challenging, nevertheless it has the advantage of enabling metal binding features to be probed over a wide range of complexation conditions. That is, the equilibrium relation between M and the various binding sites in HA is given by a distributed affinity and an ensuing stability constant K which varies with the degree of occupation of the binding sites. In line with the Eigen-based mechanism (Fig. 2), the association rate constant, k_a, has been shown to be independent of the degree of binding site coverage θ_M (see Section D2.2),[97] and thus the distribution of K is reflected in that of the dissociation rate constant, k_d.

D2.1 Intraparticulate speciation

As explained in Section B, apparent binding parameters that refer to smeared-out concentrations of all forms of M that are associated with an NP have limited meaning. The first insights into the CCD model and the framework for intraparticulate speciation were obtained from studies on metal complexes with large soil HA ($r_p \approx 80$ nm).[17-19] The high structural charge of HA at near-neutral pH has the consequence that both electrostatics and chemical affinities generally make significant contributions to the overall binding. The heterogeneous nature of HA means that the intrinsic affinity constant $\overline{K}_{int}$ increases with decreasing θ_M, whilst for sufficiently low θ_M, the electrostatic contribution to the binding remains approximately constant. The overbar notation for $\overline{K}_{int}$ signifies that the intrinsic stability represents a weighted average of all the inner-sphere complexes that are formed at the applicable θ_M. The procedure for computation of the intraparticulate speciation is detailed in our previous work.[19,24] In brief, the total concentration of M within the particle body, $c_{M,t}$, is given by:

$$c_{M,t} = c_M^D \varphi_D + (c_M^{DL} + c_{M,cond}^{DL})\varphi_{DL} + c_{MS} \qquad (44)$$

The computation is iterated until a consistent distribution of the different M species over both V_D and V_{DL} is attained that satisfies the overall charge compensation.

Examples of the distribution of the total particle-associated M(II) over its various intraparticulate species for Cd(II) and Cu(II) complexes with HA are shown by the solid bars in Fig. 11.[24] The speciation can be further differentiated on the basis of the constituent spatial zones, i.e. the Donnan volume V_D and the intraparticulate double layer V_{DL} (Fig. 3a). Within V_D, almost all of the Cd(II) and Cu(II) is in the form of inner-sphere complexes over the range of conditions shown in Fig. 11. In contrast, the speciation within V_{DL} is sensitive to θ_M, $\overline{K}_{int}$, and the ionic strength. At a θ_M of *ca.* 0.1, and an ionic strength in the medium of 10 mol m^{-3} KNO_3, the overall concentration ratio in the V_{DL} between condensed ions and inner-sphere complexes is *ca.* 3 for Cu(II) and 6 for Cd(II) (see striped bars in Fig. 11).

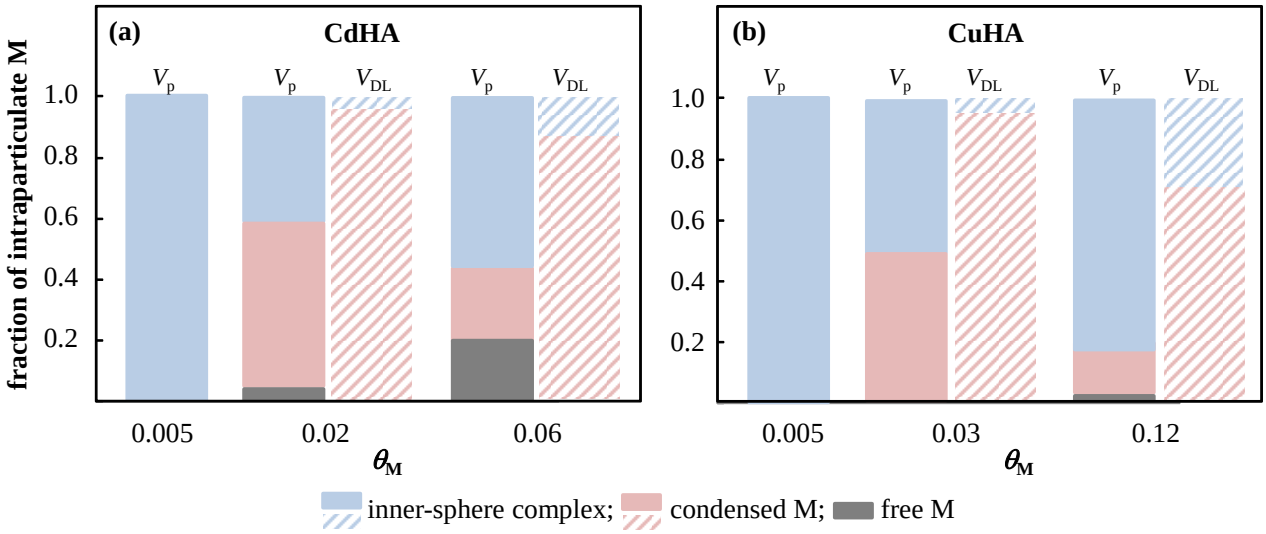

Fig. 11 Intraparticulate speciation of (a) Cd(II) and (b) Cu(II) in an aqueous dispersion of HA particles for several values of the true intraparticulate θ_M, as derived from the CCD model.[24] The fractions of the various species are expressed relative to (i) the total amount of M associated with the particle body, V_p (solid bars) and (ii) the amount of M within the DL, V_{DL} (striped bars). The bulk medium comprises 10 mol m^{-3} KNO_3 electrolyte at pH 6. For the given HA, the volume fraction ratio of the double-layer and Donnan volumes is much less than unity, i.e. a constant ψ_D can be assumed within V_D (*cf.* Fig. 3a). Figure adapted from Fig. 1 in ref. 24.

Measurements of Cd(II) and Cu(II) binding by HA in KNO_3 and $Ca(NO_3)_2$ electrolytes confirm the consistency of the CCD electrostatic model and establish a sound basis for describing the heterogeneity of the inner-sphere complexes.[24] Despite the very different intraparticulate environments in terms of net charge density and effective charge screening that prevail in the two electrolytes at ionic strengths of 10 and 100 mM, consistent $\overline{K}_{int}$ values were found at a given θ_M; Fig. 12. The dependency of $\overline{K}_{int}$ on θ_M reflects the heterogeneity of the binding sites, as described by the heterogeneity parameter Γ: $0 < \Gamma \leq 1$; $\Gamma = 1$ for the homogeneous case. The value of Γ can be obtained from the slope of a double logarithmic plot of K versus θ_M (slope = $-1/\Gamma$),[98,99] and from the shape of SSCP waves.[100,101] For HA, the Γ values derived from the $\overline{K}_{int}$ vs θ_M dependence were in excellent agreement with those obtained independently from the shape of the SSCP waves,[24] thus providing convincing support for the applicability of the CCD model for description of metal ion binding by these highly charged soft NPs.

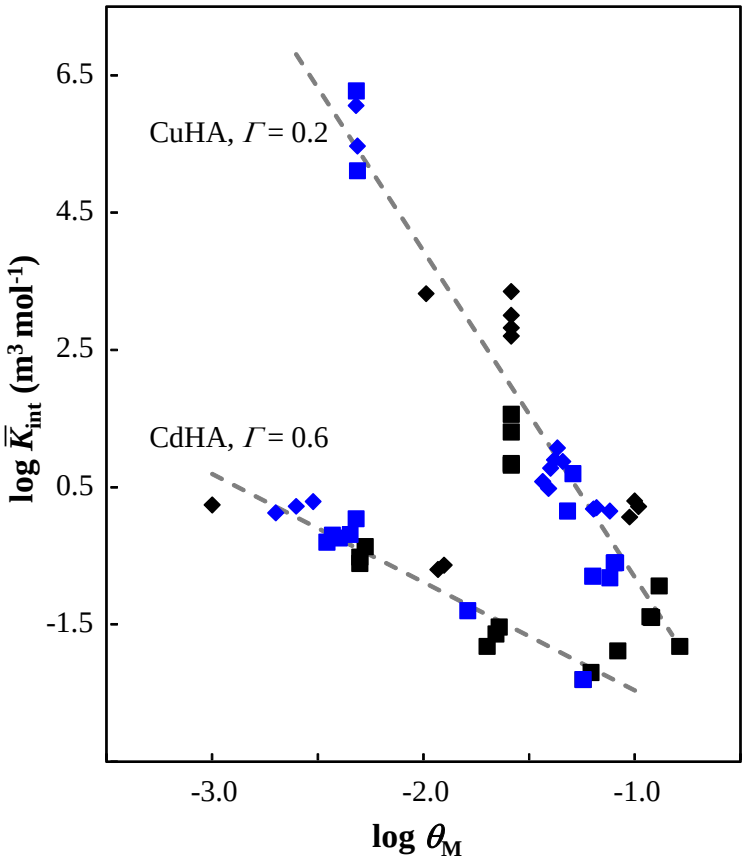

Fig. 12 Intrinsic stability constant values, log $\overline{K}_{int}$, as a function of the degree of inner-sphere complexation, log θ_M, for Cd(II) and Cu(II) complexes with HA. The data were obtained from measurements in KNO_3

electrolyte at I = 10 mol m^{-3} (solid black squares) and 100 mol m^{-3} (solid black diamonds) and in $Ca(NO_3)_2$ electrolyte at I = 10 mol m^{-3} (solid blue squares) and 100 mol m^{-3} (solid blue diamonds). The dashed grey lines, with a slope of -Γ, correspond to the best fits through all data in the respective sets of points. The figure is adapted from Fig. 3 in ref. 24.

D2.2 Chemodynamic features of metal ion binding

The step which is overall rate-limiting for the association/dissociation of a nanoparticulate metal complex depends on a range of factors, including the magnitude of the particulate electric field (charge density) and the dehydration rate of the aqueous metal ion. For a range of humic acid samples, the overall association rate constants, k_a, for Cu(II) and Ni(II) binding have been derived from collated experimental values for $\overline{K}_{int}$ and k_d as a function of θ_M .[7,28,97] Comparison of such experimentally derived k_a values with the applicable computed $k_{a,p}$ and k_a^{is} values enables the kinetic nature of the rate-limiting step in the association reaction to be identified, i.e. diffusive supply to the particle body, inner-sphere complex formation, or mixed control. For the slowly dehydrating $Ni(H_2O)_6^{2+}$ (k_w = $10^{4.5}$ s^{-1}),[102-105] the experimentally determined k_a value is in convincing agreement with the computed k_a^{is} at ionic strengths of 10 and 100 mol m^{-3}.[7] Significantly different results are obtained for the rapidly dehydrating $Cu(H_2O)_6^{2+}$ (k_w = $10^{9.6}$ s^{-1})[106-109]: mixed control is operational at an ionic strength of 100 mol m^{-3} ($k_{a,p} \approx k_a^{is}$), and whilst mixed control remains evident at I = 10 mol m^{-3}, the greater electrostatic counterion demand shifts the overall k_a in the direction of limitation by diffusive supply to the particle.[97]

D3 Effective bioavailability of nanoparticulate metal species

The theoretical framework for description of the lability of nanoparticulate metal complexes is given in Section C5, and some illustrative examples are discussed in Sections D1 and D2 for the relatively straightforward situation in which the free metal ion is consumed at a reactive interface and under conditions where there is no interaction between the M-NP entities and the interface. In order to understand and predict the bioavailability, bioaccumulation and toxicity of nanoparticulate complexes in environmental systems, it is necessary to establish the relationships between the chemodynamic and biodynamic features of M-NPs.

To date, the concentration of the free metal ion in the exposure medium is widely used as the primary predictor of bioavailability and toxicity. In the steady-state, biouptake is usually described by a Michaelis-Menten type of flux equation. The physicochemical interpretation corresponds to fast Langmuirian adsorption of the free metal ion at the external membrane, followed by a first-order rate-limiting internalisation step. There is a large body of literature that interprets metal ion accumulation and toxicity to a variety of freshwater organisms on the basis of simplified equilibrium models, e.g. the free ion activity model (FIAM) and the biotic ligand model (BLM).[110,111] However, such interpretations neglect the possible contribution of sufficiently labile complexes in the exposure medium to the biouptake flux. Equilibrium-based approaches are only valid if certain dynamic conditions are met, namely if the diffusive flux of free metal ion (*unsupported* by coupled transport of labile complex species) is greater than the biouptake flux.[112-115] This condition may be a rather severe one for aquatic organisms or ecosystems with a high degree of metal complexation, and particularly so in the presence of nanoparticulate complexes when the NP body is partially excluded from the operational reaction layer (Section C5 and Fig. 10).

It is well documented that nanoparticulate entities interact with biological interfaces, and that intact M-NP entities may be transported into cells by endocytotic processes.[116,117] In the course of the internalisation process, NPs typically acquire a protein corona,[118,119] thus 2D NPs are effectively transformed into core-shell ones. The eventual impact of an M-NP entity on an organism depends on its intracellular reactivity. Current understanding suggests that following endocytosis, most NPs are trafficked via the degradative endo/lysomal system.[120] Whilst some insights are emerging into the nature of the pathways and proteins that are responsible for intracellular trafficking of NPs,[120-122] the complexity of the involved processes means that it is not yet possible to fully elucidate the biological reactivity of M-NPs at the molecular level. This largely depends on the handling of the NPs inside the organism, the resulting tissue distribution and reactivity within specific cellular compartments. The so-called BIM-BAM approach for metal biouptake and internal biotic speciation has been developed as an operationally relevant tool to handle differences in sensitivity within and among biological species in terms of chemical speciation dynamics, exposure routes and internal handling.[123] The current model recognises pools of biologically inactive metal (BIM) and biologically active metal (BAM) inside the organism and assigns rate constants to various biological processes, including biouptake, storage,

and elimination, e.g. uptake is described in terms of exposure route and environmental conditions dependent kinetics. Upon uptake, metals enter the BAM compartment, where they can accumulate, transfer to the BIM compartment (detoxification), or be eliminated from the body. The amount of metal within the BIM and BAM compartments depends on the uptake and elimination kinetics between the organism and its environment *and* between the internal BIM and BAM compartments. Note that within an organism different BAM and BIM compartments exist: the uptake and response dynamics, together with the intrinsic sensitivity of these different compartments as a whole, determine the onset of failure and as such the toxicity thresholds. This concept also explains why metal and NP toxicity can differ by orders of magnitude among species and why a direct relationship between whole body metal or NP accumulation levels and toxicity is not generally to be expected. Application of the approach has facilitated insights into the biotic handling dynamics of metal ions;[124-126] it remains to be elucidated how the biotic machinery adapts to the presence of nanoparticulate metal species and the consequences for toxicity thresholds. Notably, the intracellular speciation and reactivity of M-NP entities, e.g. their rates of dissociation, will be influenced by the *local* concentrations of trace and major ions, pH *etc*. Intracellular conditions typically differ substantially from those in the external exposure medium, and also vary spatially within organisms, e.g. the levels of NP accumulation and the capacity to deal with them is tissue dependent. It can be envisaged that the chemodynamic features of M-NPs within the BAM compartments will be important determinants of their adverse effects on biota.

To date the majority of studies on the biological effects of metal-containing NPs have been undertaken for pure metals (e.g. Ag, Au) and metal oxides (e.g. CuO, ZnO, TiO_2). For example, the observed effects of CuO NPs on the hatching success of zebrafish has been explained in a mechanistic manner using an adverse outcome pathway (AOP) approach.[127] The main mode of action was attributed to the inhibitory effect of copper ions on the measured activity of Zebrafish Hatching Enzyme 1 (ZHE1) which is a proteolytic enzyme involved in weakening of the chorion membrane prior to hatching. The AOP involves different steps leading to the final adverse outcome, i.e. failure of hatching: (i) the release of copper ions from the NPs in the exposure solution and diffusion through chorionic pores; (ii) adsorption of NPs to the chorion membrane and release of copper ions which diffuse through the chorionic pores; (iii) the direct diffusion of NPs through the chorionic pores and release of copper ions in the perivitelline space; (iv) the non-competitive inhibition of hatching enzyme by binding of copper ions resulting in the arrest or delay of breaking of the chorion membrane; (v) mortality

of embryos through starvation or larvae through delayed feeding and development. Using a dynamic modelling approach to describe the different events it was estimated that compared to inorganic copper salts, CuO NPs may increase the uptake rate of Cu in the perivitelline space by a factor of 8.

The above example illustrates the central role of the free metal ion in explaining the toxicity of metal based NPs. In case of rapid release and complete dissolution of the NPs there will be no, or little, difference between uptake and/or toxicity when compared to inorganic salts. This is typically observed in case of ZnO NPs where toxicity between inorganic salts and NPs, when expressed on a free metal ion or dissolved concentration scale, are often very similar.[128-131] In other cases, depending on the metal based NP and the target organism, small or large differences between the uptake and toxicity of inorganic metal salts and metal based NPs have been observed.[130-137] In a number of cases these differences can be attributed to the aggregation or agglomeration status and stability of the NPs resulting in decreased metal release rates and decreased uptake or toxicity if the NPs do not directly interact with the biological interface.[138,139] However, a completely different situation exists in case of direct interaction and transport of the NPs across the biological interface.[140-142] Note that most of the earlier studies with NPs were of a short term nature and only reported acute toxicity effects. The high NP concentrations used and resulting effects on the aggregation or agglomeration states and speciation may have created exposure conditions that are never experienced under realistic conditions and also result in interactions with the biological interfaces that are unlikely to occur in nature. Therefore extrapolation of the effects of NPs observed under acute scenarios compared to chronic scenarios should therefore be treated with great caution.[143]

The nature of the interaction of NPs with the biointerface and the eventual transport across the interface depends on the physical and chemical characteristics of the NPs but also on the structural and functional organisation of the biointerface itself. The interface and barrier characteristics of bacterial, algae, plant, protozoa and animal species share mutual properties but also important differences which result in different NP adsorption characteristics, physicochemical gradients and transport pathways leading to NP internalisation.[144,145] Biological membranes and epithelial structures are also heterogeneous and patchy in terms of features and highly dynamic and responsive to changes in the external and internal environment. The direct uptake of NPs through membrane folding and endocytosis provides a route for trans-epithelial transport and small spaces between adjacent cells for para-epithelial transport.[146,147] The size and shape of the NPs are

also important considerations since they determine the space available and fitting of the NPs in the endocytic system.[148,149] When NPs enter a biological environment they often become coated by proteins forming the so-called protein corona.[150] This process may change the surface properties of the particles and the ways in which they are recognised and handled by the biological machinery.[151,152] Examples of such proteins present in circulatory fluids of animals are albumin, immunoglobulins and apolipoproteins. The coating of the NPs with immunoglobulins may promote receptor-mediated endocytosis. These types of processes are considered to play a key role in the clearance of NPs from the circulatory fluid and accumulation in specific tissues and cellular compartments.[150,153,154]

In general there is little evidence that direct uptake of NPs occurs in bacteria and yeast, but internalisation of NPs and accumulation in food vacuoles has been demonstrated in some algal species,[155] and protozoa such as *Tetrahymena*.[156] Filter feeding invertebrates such as *Daphnia* internalise NPs or their agglomerates which accumulate in the gut lumen and can interact with the gut epithelial lining.[130,157,158] The conditions in the gut lumen are under biological control and different from the external environment in terms of pH, complexation and catalytic activity, which may promote the release of metals, the formation of coronas surrounding the NPs and endocytic uptake of NPs.[159] Despite these considerations there are only a limited number of studies that provide evidence for the direct internalisation of NPs in aquatic organisms. For example, it was shown that CuO NPs ingested by *Daphnia* accumulated in the gut lumen and caused sublethal effects as demonstrated by extensive bacterial proliferation, but were apparently not transported across the gut lining.[157,158] In a study of the uptake, tissue distribution and toxicity of Ag NPs in carp there was a clear accumulation of Ag in gills, gut and liver but no evidence of Ag NP accumulation in any of these tissues.[160] Thus, although endocytic pathways provide a means for the direct uptake of NPs, the indirect routes seem to be more important to explain metal uptake and toxicity in case of metal based NPs, i.e. the release of metals in the bulk exposure phase or the release of metals from the NPs accumulating on the surface of the biointerface. This situation also appears to apply to metal ions bound to nanoparticulate complexants, i.e. M-NP entities.[161] Nonetheless, depending on the exposure scenario and especially under acute or bolus exposure scenarios the endocytic route may be critical in determining the toxicity thresholds if it is of significance in the overall uptake. The introduction of an overall relatively small quantity of metal inside certain biological compartments and subsequent trafficking including incorporation into lysosomal and other target systems may result in a very localised burst release of

metal ions but with consequences at the cellular and tissue scale.[162] For example, using a fluorescent probe approach it was demonstrated that the uptake of AgNPs in Hela and A549 cells resulted in the release of Ag^+ ions after degradation of the NPs in the acidic lysosomal environment. Under this exposure scenario the release of Ag^+ ions from the NPs in the external medium contributed little to the observed toxicity.[163] Overall this means that there are many different scenarios resulting in different and often simultaneously acting modes of uptake and toxicity. However, not all scenarios contribute equally, in terms of both uptake and toxicity, as evidenced by the range and shape of biological species sensitivity distributions for NPs. [137,164-170]

E. Conclusions and outlook

The nano-size domain, where all the chemodynamically relevant physicochemical spatial/time scales may be of comparable magnitude, has revealed many intriguing results. Significant insights have been established into the mechanistic understanding of metal ion complexation by nanoparticles. A primary issue is the importance of expressing the thermodynamic and kinetic descriptors in terms of conditions prevailing within the particle body. Concepts have been developed to delineate the intraparticulate speciation of metal ions and thus identify the intrinsic inner-sphere affinity of M-S association, as well as to describe the effect of the intraparticulate reactive site and charge distributions on the kinetics of M-NP association. The chemodynamic features of nanoparticulate metal complexes derive from the relative timescales for relaxation of the contributing electric and chemical processes. The step which is overall rate limiting in the complex formation/dissociation process depends on the properties of the NP (size, charge density, chemical functionality, softness, shape) and the target metal ion (rate of dehydration, chemical affinity), as well as the composition of the bulk medium (ionic strength, pH).

The advances in fundamental knowledge that have been established to date have great practical significance across many domains, e.g. interpretation of signals from dynamic sensors, understanding and prediction of the bioavailability of nanoparticulate metal species and of particle-mediated transport of contaminants, as well as design of smart NPs to optimize desired reactivity and minimize potential deleterious effects. For example, manipulation of the electric field of an NP is powerful tool for optimizing and tailoring its reactivity, e.g. for applications in catalysis, drug delivery, sensing, *etc*..[171-174]

Our insights into nanoparticle reactivity have also revealed a number of knowledge gaps that are awaiting (further) quantitative theoretical analysis ánd experimental verification, including:

- Elucidation of the particle shape/size dependencies of NP reactivity descriptors. The concepts developed to date have primarily addressed spherical NPs. However, NPs are manufactured in, and may transform into, a great variety of shapes. The toxicity of NPs is shape-dependent,[175-177] which can be ascribed to differences in ability to penetrate cells as well as differences in reactivity with subcellular components. The interpretation framework for NP reactivity presented herein can be applied to other geometries by adapting the various expressions as relevant, e.g. faster diffusion towards the ends of a cylindrical entity. Also the quantitative expressions developed thus far are largely applicable to NPs with radii of the order of 10 nm or greater. It is of great interest to explore the size transition zone (κr_p limit) over which the ion accumulation/reactivity evolves from the molecular scale (Eigen-Fuoss) to the multi-site NP scale with drastically enhanced activity of reactive ions within the NP body (soft, permeable particles) or at the NP surface (hard, impermeable particles).
- Description of the effect of aggregation of NPs on their reactivity, e.g. the significance of diffusion within the aggregate pores and fractal dimensions when applicable. Aggregates of NPs are common in environmental and biological systems, and typically involve mixtures of NPs and organic molecules.[178] The dedicated use of fractal dimensions may facilitate description of the reactivity of such entities.[34,179]
- Development of sophisticated electrokinetic tools to obtain key electrostatic parameters for soft NP complexes and to discriminate ion-specific effects. For example, the combination of electrophoresis with time-dependent electric/mechanical stimuli may be a fruitful means to sort out the relationship between the electrokinetic features of NPs and their interfacial adhesive characteristics.[71]
- Quantification of the chemodynamics of NP complexes in the intermediate and low charge density regimes, for which both the local potential around each charged site and the overall particle field are significant. In such cases, discretization approaches are mandatory to capture the site reactivity as a function of spatial position within the particle electric field. Also, a rigorous code for the simultaneous occurrence of electric field relaxation and chemical complexation equilibration is still unavailable.

- Development of the framework for intraparticulate speciation to include the dynamic nature of the competition between the various intraparticulate physicochemical forms of M, and the consequences for lability of the involved species at reactive interfaces (sensors and organisms). For example, there is a nuanced transition between outer-sphere, electrically condensed, and inner-sphere complexed forms of M: each species is defined by a thermodynamic stability and forms/dissociates at a certain rate, resulting in characteristic lability features at both the intraparticulate and macroscopic levels.
- Extension of the conceptual framework for the lability/bioavailability of nanoparticulate metal complexes to explicitly account for attractive and repulsive interactions between M-NP entities and the reactive interface. Under such conditions, as compared to in the absence of interactions, the M-NPs will spend more or less time in the vicinity of the reactive interface, with consequences for the magnitude of the operational reaction layer and the ensuing extent to which the particle body is excluded from the reaction layer zone.
- Derivation of the chemodynamic features pertaining to nanoparticulate metal complexes with full integration of the solvent structure and ion size-mediated electric/chemical processes operational at the NP/medium interface and within the NP body. These developments would refine understanding of particle reactivity in the nanodomain where the mean field approach is necessarily approximate.

Conflicts of interest

There are no conflicts of interest to declare.

Acknowledgements

RB and RMT conducted this work within the framework of the EnviroStress Center of Excellence at the University of Antwerp and with financial support from the BELSPO AquaStress and the UA IOF-SBO Waterside projects.

Symbols and abbreviations

Latin

A	nanoparticle surface area per unit volume of dispersion (m^2)
a	radius of impermeable core of an NP (m)

a_{os}	center-to-center distance between reactants in the outer-sphere reactant pair (m)
A_i^{os}	outer-sphere surface area of site S_i (m^2)
AOP	adverse outcome pathway
BIM	biologically inactive metal
BAM	biologically active metal
CCD	counterion condensation - Donnan
c^*	bulk concentration of background electrolyte (mol m^{-3})
c_M^*	concentration of free metal ion in the bulk solution (mol m^{-3})
c_M	intraparticulate concentration of free $M_{aq}^{z_M}$ (mol m^{-3})
$c_{M,t}$	total concentration of M within the NP body (mol m^{-3})
$\bar{c}_{M,t}$	total smeared-out concentration of all forms of M in the dispersion (mol m^{-3})
$\bar{c}_{MNP}$	sum of the smeared-out concentrations of all forms of M associated with an NP (mol m^{-3})
$c_{M•S}$	intraparticulate concentration of outer-sphere complexes (mol m^{-3})
c_{MS}	intraparticulate concentration of inner-sphere complexes (mol m^{-3})
c_{MS}^D	concentration of MS in the Donnan volume of the NP (mol m^{-3})
c_M^D	concentration of free M in the Donnan volume of the NP (mol m^{-3})
c_S^D	concentration of S in the Donnan volume of the NP (mol m^{-3})
c_{MS}^{DL}	concentration of MS in the double layer volume of the NP (mol m^{-3})
c_M^{DL}	concentration of free M in the double layer volume of the NP (mol m^{-3})
$c_{M,cond}^{DL}$	concentration of condensed M in the double layer volume of the NP (mol m^{-3})
c_S^{DL}	concentration of S in the double layer volume of the NP (mol m^{-3})
$\bar{c}_S$	average (smeared-out) concentration of free reactive sites in the whole dispersion (mol m^{-3})
$\bar{c}_{S,t}$	average (smeared-out) total concentration of reactive sites in the whole dispersion (mol m^{-3})

$\bar{c}_S^{-\lambda}$	average concentration of reactive sites in the operational reaction layer zone at a macroscopic interface (mol m^{-3})
c_S	intraparticulate concentration of binding sites (mol m^{-3})
d	thickness of the soft shell of a core-shell NP (m)
D_M	diffusion coefficient of a metal ion $M_{aq}^{z_M^+}$ in aqueous solution (m^2 s^{-1})
D_p	diffusion coefficient of a nanoparticle in aqueous solution (m^2 s^{-1})
$\bar{D}$	weighted average of the diffusion coefficients of $M_{aq}^{z_M^+}$ and NP (m^2 s^{-1})
F	Faraday constant (C mol^{-1})
$\bar{f}_B$	Boltzmann equilibrium partitioning factor
$\bar{f}_C$	condensation limit for 2+ ions in the intraparticulate double layer
f^{DL}	pre-factor for $c_{M,cond}^{DL}$
$\bar{f}_{el,a}$	electrostatic coefficient for conductive diffusion towards the NP
$\bar{f}_{el,d}$	electrostatic coefficient for conductive diffusion away from the NP
HA	humic acid
J_{dif}^*	diffusion controlled flux from bulk medium to macroscopic surface (mol m^{-2} s^{-1})
J_{kin}	kinetically controlled flux for dissociation of MS within the macroscopic reaction layer (mol m^{-2} s^{-1})
KK	Koutecký-Koryta
K_{app}	apparent stability constant for all forms of M associated with an NP based on smeared-out concentrations (m^3 mol^{-1})
K_H	Henry coefficient (m)
K_{int}	intrinsic stability constant for inner-sphere MS (m^3 mol^{-1})
$\bar{K}_{int}$	intrinsic average stability constant for inner-sphere MS (m^3 mol^{-1})
K^{os}	stability constant for an outer-sphere reactant pair (m^3 mol^{-1})

k_a	overall association rate constant ($m^3\ mol^{-1}\ s^{-1}$)
$k_{a,p}$	rate constant for diffusive supply of $M_{aq}^{z_M^+}$ to an NP ($m^3\ mol^{-1}\ s^{-1}$)
k_a^{is}	rate constant for inner-sphere complex formation from the precursor outer-sphere complex in an NP ($m^3\ mol^{-1}\ s^{-1}$)
k_a^{os}	rate constant for outer-sphere complex formation in an NP ($m^3\ mol^{-1}\ s^{-1}$)
$k_{d,p}$	rate constant for diffusion of $M_{aq}^{z_M^+}$ away from a 3D NP (s^{-1})
k_d^{is}	rate constant for inner-sphere complex dissociation in a 3D NP (s^{-1})
k_d^{os}	rate constant for outer-sphere complex dissociation in a 3D NP (s^{-1})
k_w	inner-sphere dehydration rate constant of hydrated metal ions (s^{-1})
ℓ_C	average intraparticulate distance between structural charges (m)
ℓ_{DL}	intraparticulate double-layer thickness (m)
ℓ_S	average intraparticulate distance between charged reactive sites (m)
$< \ell_S >$	distribution-dependent characteristic length scale (m)
$\mathcal{L}_{NP}$	lability parameter for nanoparticulate MS at a macroscopic reactive interface
M	metal ion
$M_{aq}^{z_M}$	free hydrated metal ion
$M_{aq}^{z_M} \bullet S$	outer-sphere associate of $M_{aq}^{z_M^+}$ and S
M_{cond}	condensed metal ion
MS	inner-sphere complex between M and S
N_{Av}	Avogadro's constant (mol^{-1})
N_S	number of reactive sites per particle
NP	nanoparticle
P_{site}^i	probabilistic M partitioning function
Q	particle charge (C)
r_0	radius of the sensing (bio)surface (m)

r^{os}	radius of an outer-sphere associate between $M_{aq}^{z_M}$ and an individual site S (m)
r_p	particle radius (m)
R	gas constant (J K^{-1} mol^{-1})
$R_{a,p}$	rate of diffusive supply of $M_{aq}^{z_M^+}$ towards an NP (mol m^{-3} s^{-1})
R_a^{is}	rate of inner-sphere complex formation in an NP (mol m^{-3} s^{-1})
$R_{d,p}$	rate of diffusive efflux of $M_{aq}^{z_M^+}$ away from an NP (mol m^{-3} s^{-1})
R_d^{is}	rate of inner-sphere complex dissociation in an NP (mol m^{-3} s^{-1})
S	reactive site
SSCP	stripping chronopotentiometry at scanned deposition potential
T	temperature (K)
$\boldsymbol{U}$	dimensionless electric energy
$\boldsymbol{U}^{os}$	dimensionless electrostatic potential between $M_{aq}^{z_M^+}$ and an individual site S in an outer-sphere associate
$\boldsymbol{U}_p$	dimensionless electrostatic potential between the particle body and the bulk medium
V_D	volume of the particle Donnan zone (m^3)
V_{DL}	volume of the intraparticulate double-layer (m^3)
V^{os}	volume of an outer-sphere associate between $M_{aq}^{z_M}$ and an individual site S (m^3)
V_{shell}	volume of the soft shell of an NP (m^3)
V_p	volume of the entire body of an NP (m^3)
z_M	charge on a metal ion

Greek

Γ	heterogeneity parameter
Γ_M	surface concentration of $M_{aq}^{z_M}$ (mol m^{-2})
Γ_{MS}	surface concentration of MS (mol m^{-2})

Γ_S	surface concentration of S (mol m^{-2})
δ_{NP}	steady-state NP diffusion layer thickness (m)
$\overline{\delta}$	mean diffusion layer thickness at a macroscopic interface for $M_{aq}^{z_M}$ and MS (m)
θ_M	ratio of concentrations of inner-sphere complexes and reactive sites
κ^{-1}	screening length in the bulk electrolyte medium (m)
λ_{NP}	thickness of the intraparticulate reaction layer for a 3D nanoparticle (m)
$\overline{\lambda}$	thickness of the operational reaction layer at the macroscopic interface (m)
ρ_p	volume charge density due to structural charges in an NP body (C m^{-3})
φ_{DL}	volume fraction of the particle double layer zone in the dispersion
φ_D	volume fraction of the particle Donnan zone in the dispersion
ψ_D	Donnan potential (V)
ψ_p	average electrostatic potential difference between the particle body and the bulk medium (V)

References

1 J. H. A. M. Wonders and H. P. van Leeuwen, *J. Electroanal. Chem.* 1996, **401**, 103-112.

2 C. M. S. Botelho, R. A. R. Boaventura and M. L. S. S. Gonçalves, *Anal. Chim. Acta* 2002, **462**, 73-85.

3 C. M. S. Botelho, R. A. R. Boaventura and M. L. S. S. Gonçalves, *Electroanalysis* 2002, **14**, 1713-1721.

4 J. P. Pinheiro, M. Minor and H. P. van Leeuwen, *Langmuir* 2005, **21**, 8635-8642.

5 H. P. van Leeuwen and J. Buffle, *Environ. Sci. Technol.* 2009, **43**, 7175-7183.

6 H. P. van Leeuwen, R. M. Town and J. Buffle, *Langmuir* 2011, **27**, 4514-4519.

7 H. P. van Leeuwen, J. Buffle, J. F. L. Duval and R. M. Town, *Langmuir* 2013, **29**, 10297-10302.

8 J. Crank, *The Mathematics of Diffusion*, Oxford Science Publications, Oxford, 1979.

9 H. P. van Leeuwen, J. Buffle and R. M. Town, *Langmuir* 2012, **28**, 227-234.

10 J. Heyrovský and J. Kůta, *Principles of Polarography*, Academic Press, New York, 1966.

11 R. Brdička and K. Wiesner, *Collect. Czech. Chem. Commun*. 1947, **12**, 39-63.

12 J. Koutecký, *Collect. Czech. Chem. Commun.* 1953, **18**, 597-610.

13 H. P. van Leeuwen and R. M. Town, *J. Solid State Electrochem.* 2016, **20**, 3255-3262.

14 R. M. Town, J. P. Pinheiro and H. P. van Leeuwen, *Langmuir* 2017, **33**, 527-536.

15 K. Krishnan and R. A. Plane, *J. Am. Chem. Soc.* 1968, **90**, 3195-3200.

16 L. A. Clapp, C. J. Siddons, J. R. Whitehead, D. G. van Derveer, R. D. Rogers, S. T. Griffin, S. B. Jones and R. D. Hancock, *Inorg. Chem.* 2005, **44**, 8495-8502.

17 H. P. van Leeuwen and R. M. Town, *Environ. Chem.* 2016, **13**, 76-83.

18 R. M. Town and H. P. van Leeuwen, *Phys. Chem. Chem. Phys.* 2016, **18**, 10049-10058.

19 R. M. Town and H. P. van Leeuwen, *Phys. Chem. Chem. Phys.* 2016, **18**, 18024-18032.

20 R. M. Fuoss, *J. Am. Chem. Soc.* 1958, **80**, 5059-5061.

21 G. S. Manning, *Biophys. Chem.* 1977, **7**, 95-102.

22 G. S. Manning, *Q. Rev. Biophys.* 1978, **2**, 179-246.

23 M. Eigen, *Pure Appl. Chem.* 1963, **6**, 97-115.

24 R. M. Town and H. P. van Leeuwen, *J. Phys. Chem A* 2016, **120**, 8637-8644.

25 R. M. Town, J. Buffle, J. F. L. Duval and H. P. van Leeuwen, *J. Phys. Chem. A* 2013, **117**, 7643-7654.

26 F. M. M. Morel and J. G. Hering, *Principles and Applications of Aquatic Chemistry*, Wiley-Interscience, New York, 1993.

27 H. P. van Leeuwen, *Langmuir* 2008, **24**, 11718-11721.

28 R. M. Town, H. P. van Leeuwen and J. Buffle, *Environ. Sci. Technol.* 2012, **46**, 10487-10498.

29 P. Debye, *Trans. Electrochem. Soc.* 1942, **82**, 265-272.

30 M. von Smoluchowski, *Phys. Z.* 1916, **17**, 585-599.

31 M. von Smoluchowski, *Z. Phys. Chem.* 1917, **92**, 129-168.

32 J. F. L. Duval and H. P. van Leeuwen, *J. Phys. Chem. A* 2012, **116**, 6443-6451.

33 J. F. L. Duval, *Phys. Chem. Chem. Phys.* 2017, **19**, 11802-11815.

34 Z. Zhang, J. Buffle and D. Alemani, *Environ. Sci. Technol.* 2007, **41**, 7621-7631.

35 R. P. Buck, *J. Electroanal. Chem.* 1969, **23**, 219-240.

36 A. J. Bard and L. R. Faulkner, *Electrochemical Methods. Fundamentals and Applications*, 2nd ed., Wiley, New York, 2001.

37 J. Lyklema, *Fundamentals of Interface and Colloid Science; Vol. IV: Particulate Colloids*, Elsevier, Amsterdam, 2005.

38 J. F. L. Duval, *J. Phys. Chem. A* 2009, **113**, 2275-2293.

39 L. P. Yezek and H. P. van Leeuwen, *Langmuir* 2005, **21**, 10342-10347.

40 P. D. Polyakov and J. F. L. Duval, *Phys. Chem. Chem. Phys.* 2014, **16**, 1999-2010.

41 J. Lyklema, *Fundamentals of Interface and Colloid Science; Vol. I: Fundamentals*, Academic Press, London, 1991.

42 H. M. Schey, *Div, Grad, Curl, and All That: an Informal Text on Vector Calculus*, 3rd edn, W. W. Norton, New York, 1997.

43 H. Ohshima, *Adv. Colloid Interface Sci.* 1995, **62**, 189-235.

44 J. F. L. Duval, *Langmuir* 2005, **21**, 3247-3258.

45. J. Buffle, Z. Zhang and K. Startchev, *Environ. Sci. Technol.* 2007, **41**, 7609-7620.

46 M. O. von Stackelberg, M. Pilgram, and V. Toome, *Z. Elektrochem*. 1953, **57**, 342−350.

47 H. P. van Leeuwen, *Electroanalysis* 2001, **13**, 826-830.

48 J. Koutecký, and J. Koryta, *Electrochim. Acta* 1961, **3**, 318-339.

49 J. Koryta, J. Dvorak and L. Kavan, *Principles of Electrochemistry*, 2nd edn. Wiley, Chichester, 1993.

50 H. P. van Leeuwen, J. Puy, J. Galceran and J. Cecília, *J. Electroanal. Chem.* 2002, **526**, 10-18.

51 H. P. van Leeuwen and R. M. Town, *J. Electroanal. Chem.* 2006, **587**, 148-154.

52 J. Buffle, K. Startchev and J. Galceran, *Phys. Chem. Chem. Phys*. 2007, **9**, 2844-2855.

53 H. P. van Leeuwen and R. M. Town, *Collect. Czech. Chem. Commun*. 2009, **74**, 1543-1557.

54 J. F. L. Duval, R. M. Town and H. P. van Leeuwen, *J. Phys. Chem. C* 2017, submitted.

55 H. P. van Leeuwen, R. M. Town, J. Buffle, R. F. M. J. Cleven, W. Davison, J. Puy, W. H. van Riemsdijk and L. Sigg, *Environ. Sci. Technol*. 2005, **39**, 8545-8556.

56 Z. Zhang, J. Buffle and H. P. van Leeuwen, *Langmuir* 2007, **23**, 5216-5226.

57 V. G. Levich, *Physicochemical Hydrodynamics*, Prentice-Hall, Englewood Cliffs, 1962.

58 P. A. Hassan, S. Rana and G. Verma, *Langmuir* 2015, **31**, 3-12.

59 T. Zheng, S. Bott and Q. Huo, *ACS Appl. Mater. Interfaces*, 2016, **8**, 21585-21594.

60 J. Gapinski, M. Jarzębski, J. Buitenhuis, T. Deptula, J. Mazuryk and A. Patkowski, *Langmuir* 2016, **32**, 2482-2491.

61 K. Koynov and H. -J. Butt, *Curr. Opin. Coll. Interf. Sci.* 2012, **17**, 377-387.

62 L. Shang and G. U. Nienhaus, *Acc. Chem. Res.* 2017, **50**, 387-395.

63 P. Hole, K. Sillence, C. Hannell, C. M. Maguire, M. Roesslein, G. Suarez, S. Capracotta, Z. Magdolenova, L. Horev-Azaria, A. Dybowska, L. Cooke, A. Haase, S. Contal, S. Manø, A. Vennemann, J. -J. Sauvain, K. C. Staunton, S. Anguissola, A. Luch, M. Dusinska, R. Korenstein, A. C. Gutleb, M. Wiemann, A. Prina-Mello, M. Riediker and P. Wick, *J. Nanopart. Res.* 2013, **15**:2101.

64 K. Mehrabi, B. Nowack, Y. A. R. Dasilva and D. M. Mitrano, *Environ. Sci. Technol.* 2017, **51**, 5611-5621.

65 M. Baalousha, B. Stolpe and J. R. Lead, *J. Chrom. A* 2011, **1218**, 4078-4103.

66 C. Contado, *Anal. Bioanal. Chem.* 2017, **409**, 2501-2518.

67 M. Plaschke, T. Schafer, T. Bundschuh, T. N. Manh, R. Knopp, H. Geckeis and J. I. Kim, *Anal. Chem.* 2001, **73**, 4338-4347.

68 R. F. Domingos, M. A. Baalousha, Y. Ju-Nam, M. M. Reid, N. Tufenkji, J. R. Lead, G. G. Leppard and K. J. Wilkinson, *Environ. Sci. Technol.* 2009, **43**, 7277-7284.

69 Y. Dieckmann, H. Cölfen, H; Hofmann and A. Petri-Fink, *Anal. Chem.* 2009, **81**, 3889-3895.

70 J. F. L. Duval and H. Ohshima, *Langmuir* 2006, **22**, 3533-3546.

71 J. F. L. Duval and F. Gaboriaud, *Curr. Opin. Coll. Interf. Sci.* 2010, **15**, 184-195.

72 J. Buffle and M. L. Tercier-Waeber, In: J. Buffle and G. Horvai (eds), *In Situ Monitoring of Aquatic Systems: Chemical Analysis and Speciation*, John Wiley & Sons: Chchester, 2000, pp. 279-405.

73 W. Davison and H. Zhang, *Environ. Chem.* 2012, **9**, 1-13.

74 J. Galceran and J. Puy, *Environ. Chem.* 2015, **12**, 112-122.

75 L. Tomaszewski, J. Buffle and J. Galceran, *Anal. Chem.* 2003, **75**, 893-900.

76 P. Gunkel-Grillon and J. Buffle, *Analyst* 2008, **133**, 954-961.

77 L. Weng, W. H. van Riemsdijk and E. J. M. Temminghoff, *Anal. Chem.* 2005, **77**, 2582-2861.

78 L. Weng, W. H. van Riemsdijk and E. J. M. Temminghoff, *Environ. Sci. Technol.* 2010, **44**, 2529-2534.

79 R. M. Town and H. P. van Leeuwen, *Environ. Chem.* 2014, **11**, 196-205.

80 H. P. van Leeuwen and R. M. Town, *J. Electroanal. Chem.* 2002, **536**, 129-140.

81 R. M. Town and H. P. van Leeuwen, *J. Electroanal. Chem.* 2003, **541**, 51-65.

82 H. P. van Leeuwen and R. M. Town, *Environ. Sci. Technol.* 2003, **37**, 3945-3952.

83 R. M. Town and H. P. van Leeuwen, *Electroanalysis* 2004, **16**, 458-471.

84 H. P. van Leeuwen and R. M. Town, *J. Electroanal. Chem.* 2003, **556**, 93-102.

85 J. Galceran, E. Companys, J. Puy, J. Cecília and J. L. Garcés, *J. Electroanal. Chem.* 2004, **566**, 95-109.

86 H. P. van Leeuwen and R. M. Town, *J. Electroanal. Chem.* 2004, **561**, 67-74.

87 R. M. Town, P. Chakraborty and H. P. van Leeuwen, *Environ. Chem.* 2009, **6**, 170-177.

88 J. F. L. Duval, J. P. S. Farinha and J. P. Pinheiro, *Langmuir* 2013, **29**, 13821-13835.

89 S. Tripathi, D. Champagne and N. Tufenkji, *Environ. Sci. Technol.* 2012, **46**, 6942-6949.

90 R. Cohen and C. N. Sukenik, *Coll Surf. A.* 2016, **504**, 242-251.

91 S. M. Bradford, E. A. Fisher and M. -V. Meli, *Langmuir* 2016, **32**, 9790-9796.

92 L. -J. A. Ellis, E. Valsami-Jones, J. R. Lead and M. Baalousha, *Sci. Total Environ.* 2016, **568**, 95-106.

93 K. A. Huynh and K. L. Chen, *Environ. Sci. Technol.* 2011, **45**, 5564-5571.

94 J. H. A. M. Wonders, *Electrochemical Metal Speciation in Colloidal Dispersions*, PhD thesis, Wageningen University, The Netherlands, 1995.

95 J. Heyrovský and J. Kůta, *Principles of Polarography*, Academic Press, New York, 1966.

96 J. F. L. Duval, K. J. Wilkinson, H. P. van Leeuwen and J. Buffle, *Environ. Sci. Technol.* 2005, **39**, 6435-6445.

97 R. M. Town, J. F. L. Duval, J. Buffle and H. P. van Leeuwen, *J. Phys. Chem A* 2012, **116**, 6489-6496.

98 J. Buffle, *Complexation Reactions in Aquatic Systems: an Analytical Approach*, Ellis Horwood, Chichester, 1988.

99 M. Filella, J. Buffle and H. P. van Leeuwen, *Anal. Chim. Acta* 1990, **232**, 209-223.

100 R. M. Town and H. P. van Leeuwen, *Aust. J. Chem.* 2004, **57**, 983-992.

101 H. P. van Leeuwen and R. M. Town, *Environ. Sci. Technol.* 2003, **37**, 3945-3952.

102 T. J. Swift and R. E. Connick, *J. Chem. Phys.* 1962, **37**, 307-320.

103 A. G. Desai, H. W. Dodgen and J. P. Hunt, *J. Am. Chem. Soc.* 1969, **91**, 5001-5004.

104 D. Rabien and G. Gordon, *Inorg. Chem.* 1969, **8**, 395-397.

105 H. A. Gazzaz, E. Ember, A. Zahl and R. van Eldik, *Dalton Trans.* 2009, 9486-9495.

106 R. Poupko and W. Luz, *J. Chem. Phys.* 1972, **57**, 3311-3318.

107 L. S. W. L. Sokol, T. D. Fink and D. B. Rorabacher, *Inorg. Chem.* 1980, **19**, 1263-1266.

108 D. H. Powell, K. Helm and A. E. Merbach, *J. Chem. Phys.* 1991, **95**, 9258-9265.

109 W. B. Lewis and M. J. Alei, *J. Chem. Phys.* 1966, **44**, 2409-2417.

110 P. G. C. Campbell, In: *Metal Speciation and Bioavailability in Aquatic Systems*, IUPAC Series on Analytical and Physical Chemistry of Environmental Systems, Vol. 3, A. Tessier & D.R. Turner (vol. eds), Wiley, New York, pp. 45-102, 1995.

111 V. Slaveykova and K. J. Wilkinson, *Environ. Chem*. 2005, **2**, 9-24.

112 H. P. van Leeuwen, *Environ. Sci. Technol.* 1999, **33**, 3743-3748.

113 S. Jansen, R. Blust and H. P. van Leeuwen, *Environ. Sci. Technol.* 2002, **36**, 2164-2170.

114 J. F. L. Duval, *Phys. Chem. Chem. Phys.* 2016, **18**, 9453-9469.

115 J. F. L. Duval, R. M. Présent and E. Rotureau, *Phys. Chem. Chem. Phys.* 2016, **18**, 30415-30435.

116 A. Asati, S. Santra, C. Kaittanis, C. and J. M. Perez, *ACS Nano* 2010, **4**, 5321-5331.

117 Z. Wang, N. Li, J. Zhao, J. C. White, P. Qu and B. Xing, *Chem. Res. Toxicol.* 2012, **25**, 1512-1521.

118 M. P. Monopoli, C. Aberg, A. Salvati and K. Dawson, *Nature Nanotech.* 2012, **7**, 779-786.

119 F. Bertoli, D. Garry, M. P. Monopoli, A. Salvati and K. A. Dawson, *ACS Nano* 2016, **10**, 10471-10479.

120 A. Panarella, M. G. Bexiga, G. Galea, E. D. O'Neill, A. Salvati, K. A. Dawson and J. C. Simpson, *Sci. Rep.* 2016, **6**:28865.

121 R. Duncan and S. C. W. Richardson, *Mol. Pharmaceutics* 2012, **9**, 2380-2402.

122 M. H. Kafshgari, F. J. Harding and N. H. Voelcker, *Curr. Drug Deliv.* 2015, **12**, 63-77.

123 W. J. Adams, R. Blust, U. Borgmann, K. V. Brix, D. K. DeForest, A. S. Green, J. S. Meyer, J. C. McCeer, P. R. Paquin, P. S. Rainbow and C. M. Wood, *Integr. Environ. Assess. Manag.* 2011, **7**, 75-98.

124 I. Komjarova and R. Blust, *Environ. Sci. Technol.* 2009, **43**, 7225-7229.

125 I. Komjarova and R. Blust, *Environ. Sci. Technol.* 2009, **43**, 7958-7963.

126 M. Eyckmans, R. Blust and G. De Boeck, *Aquat. Toxicol.* 2012, **118-119**, 97-107.

127 E. B. Muller, S. Lin and R. M. Nisbet, *Environ. Sci. Technol.* 2015, **49**, 11817-11824.

128 N. Adam, C. Schmitt, J. Galceran, E. Companys, A. Vakurov, R. Wallace, D. Knapen and R. Blust, *Nanotoxicology* 2014, **8**, 709-717.

129 N. Adam, F. Leroux, D. Knapen, S. Bals and R. Blust, *Environ. Poll.* 2014, **194**, 130-137.

130 N. Adam, F. Leroux, D. Knapen, S. Bals and R. Blust, *Water Res.* 2015, **68**, 249-261.

131 N. Adam, L. Vergauwen, R. Blust and D. Knapen, *Environ. Res.* 2015, **138**, 82-92.

132 H. C. Poynton, J. M. Lazorchak, C. A. Impellitteri, M. E. Smith, K. Rogers, M. Patra, K. A. Hammer, H. J. Allen and C. D. Vulpe, *Environ. Sci. Technol.* 2011, **45**, 762-768.

133 T. Gomes, J. P. Pinheiro, I. Cancio, C. G. Pereira, C. Cardoso and M. J. Bebianno, *Environ. Sci. Technol.* 2011, **45**, 9356-9362.

134 B. J. Shaw and R. D. Handy, *Environ. Internat.* 2011, **37**, 1083-1097.

135 D. A. Notter, D. M. Mitrano, and B. Nowack, *Environ. Toxicol. Chem.* 2014, **33**, 2733-2739.

136 A. Ivask, K. Juganson, O. Bondarenko, M. Mortimer, V. Aruoja, K. Kasemets, I. Blinova, M. Heinlaan, V. Slaveykova and A. Kahru, *Nanotoxicology* 2014, **8**, 57-71.

137 N. Adam, C. Schmitt, L. De Bruyn, D. Knapen and R. Blust, *Sci. Total Environ.* 2015, **526**, 233-242.

138 N. M. Franklin, N. J. Rogers, S. C. Apte, G. E. Batley, G. E. Gadd and P. S. Casey, *Environ. Sci. Technol.* 2007, **41**, 8484-8490.

139 A. M. Abdelmonem, B. Pelaz, K. Kantner, N. C. Bigall, P. del Pino and W. J. Parak, *J. Inorg. Biochem.* 2015, **153**, 334-338.

140 S. T. Stern, P. P. Adiseshaiah and R. M. Crist, *Part. Fibre Toxicol.* 2012, **9**:20.

141 R. Behra, L. Sigg, M. J. D. Clift, F. Herzog, M. Minghetti, B. Johnston, A. Petri-Fink and B. Rothen-Rutishauser, *J. R. Soc. Interface* 2013, **10**: 20130396.

142 J. Hua, M. G. Vijver, F. Ahmad, M. K. Richardson and W. J. G. M. Peijnenburg, *Environ. Toxicol. Chem.* 2014, **33**, 1774-1782.

143 K. Juganson, A. Ivask, I. Blinova, M. Mortimer and A. Kahru, *Beilstein J. Nanotechnol.* 2015, **6**, 1788-1804.

144 A. E. Nel, L. Mädler, D. Velegol, T. Xia, E. M. V. Hoek, P. Somasundaran, F. Klaessig, V. Castranova and M. Thompson, *Nature Mater.* 2009, **8**, 543-557.

145 C. M. Beddoes, C. P. Case and W. H. Briscoe, *Adv. Colloid Interf. Sci.* 2015, **218**, 48-68.

146 R. Duncan and S. C. W. Richardson, *Mol. Pharmaceutics* 2012, **9**, 2380-2402.

147 Y. Yue, R. Behra, L. Sigg, M. J. -F. Suter, S. Pillai and K. Schirmer, *Environ. Sci.: Nano* 2016, **3**, 1174-1185.

148 J. T. Buchman, M. J. Gallagher, C. -T. Yang, X. Zhang, M. O. P. Krause, R. Hernandez and G. Orr, *Environ. Sci.: Nano* 2016, **3**, 696-700.

149 A. Vollrath, A. Schallon, C. Pietsch, S. Schubert, T. Nomoto, Y. Matsumoto, K. Kataoka and U. S. Schubert, *Soft Matt.* 2013, **9**, 99-108.

150 D. Docter, D. Westmeier, M. Markiewicz, S. Stolte, S. K. Knauer and R. H. Stauber, *Chem. Soc. Rev.* 2015, **44**, 6094-6121.

151 C. D. Walkey and W. C. W. Chan, *Chem. Soc. Rev.* 2012, **41**, 2780-2799.

152 C. Ge, J. Tian, Y. Zhao, C. Chen, R. Zhou and Z. Chai, *Arch. Toxicol.* 2015, **89**, 519-539.

153 A. Albanese, C. D. Walkey, J. B. Olsen, H. Guo, A. Emilia and W. C. W. Chan, *ACS Nano* 2014, **8**, 5515-5526.

154 L. Shang, L. Yang, J. Seiter, M. Heinle, G: Brenner-Weiss, D. Gerthsen and G. U. Nienhaus, *Adv. Mater. Interfaces* 2014, **1**, 1300079.

155 Z. Wang, J. Li, J. Zhao and B. Xing *Environ. Sci. Technol.* 2011, **45**, 6032-6040.

156 M. Mortimer, A. Kahru and V. I. Slaveykova, *Environ. Poll.* 2014, **190**, 58-64.

157 F. R. Khan, G. M. Kennaway, M. -N. Croteau, A. Dybowska, B. D. Smith, A. J. A. Nogueira, P. S. Rainbow, S. N. Luoma and E. Valsami-Jones, *Chemosphere* 2014, **100**, 97-104.

158 M. Heinlaan, A. Kahru, K. Kasemets, B. Arbeille, G. Prensier and H. -C. Dubourguier, *Water Res.* 2011, **45**, 179-190.

159 J. García-Alonso, F. R. Khan, S. K. Misra, M. Turmaine, B. D. Smith, P. S. Rainbow, S. N. Luoma and E. Valsami-Jones, *Environ. Sci. Technol.* 2011, **45**, 4630-4636.

160 M. -H. Jang, W. -K. Kim, S. -K. Lee, T. B. Henry and J. -W. Park, *Environ. Sci. Technol.* 2014, **48**, 11568-11574.

161 W. -W. Yang, A. -J. Miao and L. -Y. Yang, *PLoS ONE* 2012, **7**, e32300.

162 S. Sabella, R. P. Carney, V. Brunetti, M. A. Malvindi, N. Al-Juffali, G. Vecchio, S. M. Janes, O. M. Bakr, R. Cingolani, F. Stellacci and P. P. Pompa, *Nanoscale* 2014, **6**, 7052-7061.

163 V. De Matteis, M. A. Malvindi, A. Galeone, V. Brunetti, E. De Luca, S. Kote, P. Kshirsagar, S. Sabella, G. Bardi and P. P. Pompa, *Nanomedicine* 2015, **11**, 731-739.

164 T. L. Botha, T. E. James and V. Wepener, *J. Nanomaterials* 2015, 986902.

165 C. Coll, D. Notter, F. Gottschalk, T. Sun, C. Som and B. Nowack, *Nanotoxicology* 2016, **10**, 436-444.

166 K. L. Garner, S. Suh, H. S. Lenihan and A. A. Keller, *Environ. Sci. Technol.* 2015, **49**, 5753-5759.

167 J. I. Kwak, R. Cui, S. -H. Nam, S. W. Kim, Y. Chae and Y. -J. An, *Nanotoxicology* 2016, **10**, 521-530.

168 S. -H. Nam, Y. -J. Shin, W. -M. Lee, S. W. Kim, J. I. Kwak, S. -J. Yoon and Y. -J. An, *Nanotoxicology* 2015, **9**, 326-335.

169 E. Semenzin, E. Lanzellotto, D. Hristozov, A. Critto, A. Zabeo, E. Guibilato and A. Marcomini, *Environ. Toxicol. Chem.* **34**, 2644-2659.

170 Y. Wang, A. Kalinina, T. Sun and B. Nowack, *Sci. Total Environ.* 2016, **545-546**, 67-76.

171 D. E. Park, S. J. Lee, J. -H. Lee, M. Y. Choi and S. W. Han, *Chem. Phys. Lett.* 2010, **484**, 254-257.

172 K. Kwak, S. S. Kumar and D. Lee, *Nanoscale* 2012, **4**, 4240-4246.

173 Z. Liang, C. Wang, Z. Tong, W. Ye and S. Ye, *React. Funct. Polym.* 2005, **63**, 85-94.

174 M. Bieja, E. Palleau, S. Sistach, X. Zhao, L. Ressier, C. Mingotaud, M. Destarac and J. -D. Marty, *J. Mater. Chem.* 2010, **20**, 9433-9442.

175 L. M. Gilbertson, E. M. Albalghiti, Z. S. Fishman, F. Perreault, C. Corredor, J. D. Posner, M. Elimelech, L. D. Pfefferle and J. B. Zimmerman, *Environ. Sci. Technol.* 2016, **50**, 3975-3984.

176 M. Bhamidipati and L. Fabris, *Bioconjugate Chem.* 2017, **28**, 449-460.

177 V. Forest, L. Leclerc, J. -F. Hochepied, A. Trouvé, G. Sarry and J. Pourchez, *Toxicol. In Vitro* 2017, **38**, 136-141.

178 H. Wang, A. S. Adeleye, Y. Huang, F. Li and A. A. Keller, *Adv. Coll. Interf. Sci.* 2015, **226**, 24-36.

179 H. Guénet, M. Davranche, D. Vantelon, J. Gigault, S. Prévost, O. Taché, S. Jaksch, M. Pédrot, V. Dorcet, A. Boutier and J. Jestin, *Environ. Sci.: Nano*, 2017, **4**, 938-954.